Imaging the columnar functional organization of human area MT+ to axis-of-motion stimuli using VASO at 7 Tesla

Alessandra Pizzuti[a,b,*], Laurentius (Renzo) Huber[a], Omer Faruk Gulban[a,b], Amaia Benitez-Andonegui[c], Judith Peters[a], Rainer Goebel[a,b,*]

[a]*Department of Cognitive Neuroscience, Faculty of Psychology and Neuroscience, Maastricht University, Maastricht, NL,*
[b]*Brain Innovation, Maastricht, NL,*
[c]*MEG Core Facility, National Institute of Mental Health, Bethesda, USA,*

Abstract

Cortical columns of direction-selective neurons in the motion sensitive area (MT) have been successfully established as a microscopic feature of the neocortex in animals. The same property has been investigated at mesoscale (<1mm) in the homologous brain area (hMT+) in living humans by using ultra-high field fMRI. Despite the reproducibility of the selective response to axis-of-motion stimuli, clear quantitative evidence for the columnar organization of hMT+ is still lacking. Using cerebral blood volume (CBV)-sensitive fMRI at 7 Tesla with submillimeter resolution and high spatial specificity to microvasculature, we investigate the columnar functional organization of hMT+ (V5) in 5 participants perceiving axis-of-motion stimuli for both blood oxygenation level dependent (BOLD) and vascular space occupancy (VASO) contrast mechanisms provided by the used Slab-Selective Slice Inversion (SS-SI)-VASO sequence. With the development of a new searchlight-like algorithm for column detection, we provide the first quantitative columnarity map that characterizes the entire 3D hMT+ volume. We demonstrate the advantage of using CBV-sensitive fMRI to detect mesoscopic cortical features by showing, through our new voxel-wise measures of sensitivity and specificity, the higher specificity of axis-of-motion cortical columns detected by VASO compared to BOLD contrast. These voxel-wise metrics also provide further insights on how to mitigate the highly debated draining veins effect. We conclude that using CBV-VASO fMRI together with voxel-wise measurements of sensitivity, specificity and columnarity offers a promising avenue to quantify the mesoscopic organization of hMT+ with respect to axis-of-motion stimuli. Furthermore, our approach and methodological developments are generalizable and applicable to other human brain areas where similar mesoscopic research questions are addressed.

Keywords: columns, 7 Tesla, fMRI, V5-hMT+, VASO, CBV, layers

1. Introduction

An important task of the visual system is to recognize moving objects in a dynamic environment. The macaque middle temporal (MT) area and its homologue in humans (hMT+, V5) is a high order cortical visual area sensitive to

*Corresponding authors.

the direction of motion (Watson et al., 1993; Born and Bradley, 2005; Zeki, 1974; Maunsell and Van Essen, 1983; Rees et al., 2000; Zimmermann et al., 2011). It also plays an important role in constructive motion perception as revealed by illusory (e.g. apparent) motion stimuli (Goebel et al., 1998; Born and Bradley, 2005; Schneider et al., 2019). The hypothesis that the macaque extra-striate area MT is functionally organized in cortical columns similarly to V1 (Hubel and Wiesel, 1965) was supported by results from invasive electrophysiological recordings (Albright et al., 1984; Diogo et al., 2003) and optical imaging (Malonek et al., 1994). In particular, Albright et al. (1984) demonstrated in macaque MT the occurrence of a systematic relationship between the penetration angle of the electrode and the rate of change of preferred direction of motion, indicating that cells with a similar preference are arranged in vertically oriented columns (Mountcastle, 1997; Buxhoeveden and Casanova, 2002). Albright et al. also discovered that opposing directions of motion are located in neighboring columns forming larger axis-of-motion columns.

The advent of magnetic resonance imaging opened the avenue to bridge the gap to animal literature, by non-invasively investigating the functional organization of the human brain. Especially the advent of ultra high field (UHF) functional magnetic resonance imaging (fMRI) combined with recent advances in MR hardware and pulse sequences offers sub-millimeter spatial resolution (Uğurbil et al., 2003; Shmuel et al., 2007; Uludağ et al., 2009; Koopmans and Yacoub, 2019) providing a unique way to unveil mesoscopic properties underlying cognitive functions at the level of cortical layers and cortical columns (Rakic, 2008; Petro and Muckli, 2017; Ugurbil, 2016; Dumoulin et al., 2018; De Martino et al., 2018; Viessmann and Polimeni, 2021; Uğurbil, 2021; Huber et al., 2020; Cho et al., 2022). Mesoscopic 7T fMRI has already been used to investigate the columnar organization of human MT using 3D-GRASE (Zimmermann et al., 2011; De Martino et al., 2013; Oshio and Feinberg, 1992; Feinberg et al., 1995; Kemper et al., 2015) and BOLD contrast. Zimmermann et al. (2011) provided the first direct demonstration of axis of motion selectivity and tuning characteristics in the human brain together with first insights into the spatial organization of hMT. However, their columnar results can only be seen as an early approximation, since the provided limited number of samples across cortical depth could still be insufficient to capture the full arrangement of vertical columnar property. To validate and enhance previous findings, we investigate the functional organization of hMT+ in humans perceiving axis-of-motion stimuli with three novel aspects: (I) we use cerebral blood volume (CBV)-sensitive fMRI in addition to conventional BOLD fMRI, (II) we provide a new local or voxel-wise measure of sensitivity and specificity, and (III) we develop a novel method to detect, characterize and visualize cortical columns.

CBV-sensitive fMRI. We use the SS-SI VASO (Huber et al., 2014) pulse sequence to get high-resolution CBV-sensitive fMRI. The VASO sequence is more suitable for imaging mesoscopic features compared to standard gradient echo BOLD echo planar imaging (GE-BOLD EPI), since it provides higher spatial specificity to the microvasculature and it is less compromised by both oxygenation related vascular changes as well as large draining effects from vessels penetrating the cortex orthogonally or from pial veins lying on top of the gray matter surface (Duvernoy et al., 1981; Weber et al., 2008; Lauwers et al., 2008).

Local measure of sensitivity and specificity. For more precise quantification of responses, we develop a voxel-wise measure of sensitivity and specificity as an extended version of the conventional global measure (Beckett et al., 2020;

Huber et al., 2017). Global metrics summarize the behavior of an entire region of interest, whereas our local metrics provide a functional characterization for each voxel inside a region of interest, resulting in more complete information for addressing mesoscopic questions at submillimeter resolution. More specifically, our new local metrics allow to evaluate the tuning property encoded in each voxel: if a voxel is strongly tuned to a specific condition its specificity will be high and its sensitivity will be inherited by the contrast mechanism, whereas if a voxel is poorly tuned, as in the case of a voxel sampling a big vessel, the specificity will be very low while the sensitivity will be very high. The information provided by our metrics is also used to compare results from BOLD and VASO contrast mechanisms (Huber et al., 2017, 2020; Oliveira et al., 2022).

Novel method to characterize cortical columns. To overcome depth-sampling limitations (Zimmermann et al., 2011), we develop a new searchlight-like algorithm for column detection that inspects the whole cortical depth of a specific volume of interest and provides a quantitative columnarity map that is useful to detect highly-columnar patches inside the volume. The algorithm provides a new generalized framework for investigating the columnar functional organization for any cortical gray matter ribbon and it can potentially improve the replicability and comparability of columnar results across studies using a variety of columnar quantification methods (Yacoub et al., 2008; Zimmermann et al., 2011; De Martino et al., 2013, 2015; Schneider et al., 2019).

In this study we acquire ultra-high field (7 Tesla) fMRI at submillimeter isotropic resolution (0.8mm) to investigate the axis of motion cortical columns in hMT+ (V5). By using our new algorithm for column detection, we provide a quantitative columnarity map that fully characterizes the functional organization of hMT+ with respect to axis-of-motion preference. We demonstrate the advantage of using CBV-sensitive fMRI to detect mesoscopic cortical features by showing the higher specificity of axis of motion cortical columns detected by VASO compared to BOLD contrast.

2. Methods

2.1. Experimental design

Five healthy participants (4 males and 1 female, 28-34 years old) with normal or corrected-to-normal vision were recruited for the study. Participants received a monetary reward. All participants had been in an MRI scanner at least once before and were trained and experienced at maintaining fixation for long periods of time. Informed consent was obtained from each participant before conducting the experiment. The study was approved by the ethics review committee of the Faculty of Psychology and Neuroscience (ERCPN) of Maastricht University and experimental procedures followed the principles expressed in the Declaration of Helsinki. A frosted screen at the rear of the magnet was used to project the visual stimuli that participants could watch through a tilted mirror attached to the head coil. An MR compatible button box was used to register participants' responses for the attention task during the entire functional scanning procedure. In a two hour scanning session we acquired 1 run to functionally locate hMT+, 3-4 runs to map four axes of motion and an MP2RAGE scan for the structural images (only if not already available from a previous scanning session). For the hMT+ functional localizer, a standard block design paradigm was used presenting moving

dots in alternation with static dots in a circular aperture (Tootell et al., 1995). We did not separate MST from hMT (Huk et al., 2002; Kolster et al., 2010; Zimmermann et al., 2011) since we aimed to cover the whole human motion complex (hMT+). Dots traveled inwards and outwards from the center of the aperture for 10 seconds (speed = 8 degree of visual angle per second, dot size = 0.2 degree of visual angle, number of dots = 200, black dots on gray background), were followed by a stationary dots display presented for the same amount of time. A total of 27 repetitions of task-rest blocks were collected. For the axis of motion mapping, we presented dots in a circular aperture moving coherently along one of four axes (0° ↔ 180°,45° ↔ 225°, 90° ↔ 320°, 135° ↔ 315°, in both directions of motion) (Zimmermann et al., 2011) alternated with static flickering dots. Moving dot patterns (speed = 8 degrees of visual angle per second, dot size = 0.2 degree of visual angle, number of dots = 250) were presented for 24 seconds followed by a variable inter-trial interval (ITI) of 24–29 seconds to reduce functional signal carry over effects. Each motion axis block was repeated four times per run. In all conditions, a black disk (target/fixation dot) surrounded by an annulus was presented in the center of the aperture. Participants were instructed to fixate the black disk and respond through the button box every time the annulus changed color (attention task). The scripts used for the stimulus presentation were developed based on Schneider et al. (2019) and presented using the open source application PsychoPy3 (v2020.2.4) which are available on `https://github.com/27-apizzuti/AOM-VASO_project`.

2.2. MRI acquisition

Data acquisition was performed on a whole-body "classical" MAGNETOM 7T (Siemens Healthineers, Erlangen, Germany) at Scannexus B.V. (Maastricht, The Netherlands) using a 32-channel RX head-coil (Nova Medical, Wilmington, MA, USA). A second and a third order B0 shimming procedure was used to improve the homogeneity of the main magnetic field B0 in the shim volume containing the interested region. The localizer experiment was conducted using a GE EPI sequence with BOLD contrast (Moeller et al., 2010) (echo time (TE)=15 ms, nominal flip angle (FA)=55°, echo repetition time (TR)=1000 ms, multi band factor (MB)=3, 57 slices) with a whole brain field of view and a (98×98) matrix at 2 mm isotropic nominal resolution. Before the acquisition of the run, we collected 5 volumes for distortion correction with the settings specified above but opposite phase encoding (posterior-anterior). For the axis of motion mapping experiment, we used a Vascular Space Occupancy (VASO) sequence (Lu et al., 2003) optimized for 7T (Hua et al., 2013). Specifically, we used the Slab-Selective Slice Inversion (SS-SI VASO) approach (Huber et al., 2014) with a 3D EPI readout (Poser et al., 2010) at nominal isotropic voxel resolution of 0.8 mm. Previous work has shown that the 3D readout is beneficial for sub-millimeter applications (Huber et al., 2018). The in-plane field of view was 129×172 mm (162×216 matrix) for a total of 26 acquired slices. The imaging parameters were: TE=25ms, 'temporal resolution' of pairs of images=4840ms, variable flip angle scheme FA=26+°, in plane partial Fourier factor 6/8 with POCS reconstruction of 8 iterations, inversion time (TI)=1530ms for the blood nulling point and FLASH-GRAPPA=3 (Talagala et al., 2016). Variable flip angles were used to minimize T_1-related blurring along the slice direction (Huber et al., 2018). The sequence was implemented using the vendor provided IDEA environment (VB17A-UHF) and is available to download via C2P on the SIEMENS App-Store in Teamplay. The placement of the small functional slab

was guided by an online analysis of the hMT+ localizer data (general linear modeling by Siemens), to ensure a bilateral coverage of area hMT+ for every participant. The anatomical images were acquired with an MP2RAGE (magnetization prepared two rapid gradient echoes) (Marques et al., 2009) at 0.7 mm isotropic resolution (TR/TE=6000ms/2.39ms, TI=800ms/2750ms, FA=4°/5°, GRAPPA=3). MP2RAGE sequence parameters are optimized to overcome the large spatial inhomogeneity in the transmit B1 field by generating and combining in a novel fashion two different images at two different inversion times (TI1, TI2) to create T_1-weighted MP2RAGE uniform (UNI) images (Marques et al., 2009). Physiological traces of respiration and heartbeat were recorded but not used for the analysis, since we did not observe any improvements by conducting `RETROICOR` physiological noise correction during the piloting stage (Glover et al., 2000). Indeed, sub-millimeter data are expected to be in the thermal noise-dominated regime (Triantafyllou et al., 2005).

2.3. Structural data analysis

2.3.1. Preprocessing and registration

T_1-weighted UNI images with high contrast-to-noise ratio from MP2RAGE were used to guide the determination of the anatomical location of hMT+ and to derive layers in the cortical ribbon of interest. T_1-w UNI images were skull-stripped using a brain mask obtained by inputting the MP2RAGE INV2 (TI2) images to FSL BET (v.6.0.5) (Smith et al., 2004). When needed, we manually corrected the results and used Segmentator (v.1.6.0) (Gulban et al., 2018) to remove dura mater contribution. Then, we used the anatomical bias correction algorithm from SPM12 (Wellcome Trust Center for Neuroimaging, London, UK) to further reduce inhomogeneities in the T_1-w UNI images (Friston et al., 2007; Ashburner and Friston, 2005). In order to preserve the high-resolution functional data from issues of registration and interpolation while computing depth-dependent analysis (Huber et al., 2017; Guidi et al., 2020), we aligned the T_1-w UNI images to the high-resolution functional VASO data, according to `https://layerfmri.com/2019/02/11/high-quality-registration/`. The target functional slab "T_1-w EPI" was derived from the original SS-SI VASO time series by computing the inverse of signal variability that provides a good contrast between gray matter (GM) and white matter (WM) using AFNI (v.20.3.01) (Cox, 1996; Cox and Hyde, 1997) (function: `-cvar`). In ITK-SNAP (v.3.8) (Yushkevich et al., 2006) we manually aligned the T_1-w UNI whole brain images to the T_1-w EPI slab and then ran ITK-SNAP's automatic co-registration tool. Then, we used the obtained transformation matrix as input for running ANTS's "Syn" registration algorithm (v.20.3.01) (Avants et al., 2009, 2011; Madge, 2020). Finally, the T_1-w UNI images were resampled to the T_1-w EPI space using ANTS b-spline interpolation (`antsApplyTransforms -BSpline`).

2.3.2. Segmentation

Tissue segmentation is a crucial step to investigate cortical layers and columns. Since conventional segmentation packages are inadequately optimized for data with a restricted field of view, a semi-automated segmentation approach with manual intervention was used here. Therefore, although we define the functional location of hMT+ and process

functional responses to axis-of-motion stimuli in both hemispheres, we restrict depth-dependent analysis only to the left hemisphere where we get higher cross-validated activity compared to the right one (see result section "Axes of motion tuning curves confirm motion-selective behavior"). We used `-3dresample` command from AFNI (v.20.3.01) to upsample (with cubic interpolation) the processed T_1-w UNI images with an upscaling factor of 4 (nominal resolution = 0.2 mm isotropic). This step allowed a smoothed calculation of cortical features (e.g. curvature or thickness). Then, we confined the segmentation process to a "scoop of interest" in the left hemisphere: in ITK-SNAP we centered a spherical mask around the anatomically expected area hMT+. We ran FSL FAST to obtain a first definition of the CSF/GM and the GM/WM tissue borderlines. Tissue labels were carefully quality controlled and manually edited when necessary (by A.P.), and later revised independently by another expert (O.F.G.). In combination, we also used morphological operations (dilation and erosion) (Virtanen et al., 2020) to further improve the segmentation output. These operations, when applied in combination with the same parameters, remove mislabeled isolated voxels and smooth boundaries between tissues.

2.3.3. Cortical depths

Once the segmentation was completed, we used `LN2_LAYERS` program from LayNii (v2.2.1) (Huber et al., 2021) to compute, for each gray matter voxel, a normalized equi-volume cortical depth measurement (Bok, 1959; Waehnert et al., 2014) as well as a cortical thickness and a curvature value.

2.3.4. Flattening

We used `LN2_LAYERS`, `LN2_MULTILATERATE`, and `LN2_PATCH_FLATTEN` programs within LayNii (Gulban et al., 2021) to flatten our cortical patches. We first establish the center of gravity of the gray matter activated ROI (left hMT+). Then a disk of a predefined radius (see Supplementary Table 1) is grown geodesically and a local 2D coordinate system (U and V coordinates) was imposed on it (using `LN2_MULTILATERATE` program). Together with the "metric" file from `LN2_LAYERS` (D coordinate), the end result of this procedure is a full continuous mapping between flat cortex space (UVD) and the original folded cortex space (XYZ). This mapping allows us to flatten 3D chunks of cortical data (in NIfTI format) to explore mesoscopic cortical structures as it was done in previous studies (Zimmermann et al., 2011; De Martino et al., 2013; Schneider et al., 2019).

2.4. Functional data analysis: Localizer experiment

Functional localizer data were pre-processed in BrainVoyager v.22.1 (Goebel et al., 2012) as follows: slice scan time correction, motion-correction, linear trend removal and high-pass filtering (6 cycles). We corrected for EPI geometric distortion using the image registration-based method based on the opposite phase encoding direction EPI data as implemented in COPE BrainVoyager plugin (Breman et al., 2020). The same aligning procedure explained for structural images was also used to align functional localizer data to high-resolution VASO data. The registration parameters (ITK-SNAP, ANTS "Syn") were estimated matching the computed temporal mean image from localizer data (Smith et al., 2004) with T_1-w EPI and then applied to the time series using ANTS B-spline interpolation. Then,

in order to functionally define our ROI (bilateral hMT+), we calculated a voxel-wise general linear model (GLM) for each participant in BrainVoyager. The GLM was corrected for temporal auto-correlation (AR2). The model contained a single predictor for the stimulus condition "moving dots" convolved with a standard hemodynamic response function. Voxels that showed a significant response to "moving vs static dots" contrast (using a threshold (q) corrected for multiple comparisons using false discovery rate; q(FDR) < .05) were selected. Finally, we defined a bilateral hMT+ ROI, by intersecting these voxels with two spheres of 16 mm in radius (one for each hemisphere) placed inside the expected anatomical location (Zimmermann et al., 2011; Schneider et al., 2019).

2.5. Functional data analysis: Axes of motion experiment

2.5.1. Preprocessing and functional maps

Axis of motion functional data were analyzed following the optimized preprocessing pipeline for SS-SI VASO sequence `https://layerfmri.com/example-analysis-pipeline-of-layer-VASO`. For each run, the first four time points (non-steady state images) were overwritten with steady-state images. Then, we separated odd and even time points from raw data, corresponding to MR signals with and without blood nulling and we separately performed motion correction using SPM12 (Friston et al., 2007). A fourth-order spline was used for resampling to minimize blurring. For every participant, motion parameters between the two contrasts were very similar, as expected, and never higher than the nominal voxel resolution. The original time series length was restored for both blood-nulled and BOLD images using 7^{th} order polynomial interpolation method before multiple runs were averaged to minimize noise amplification in the next processing steps. Dynamic division of blood-nulled and BOLD volumes was performed to generate VASO images with reduced BOLD contrast contamination (LayNii `LN_BOCO` program). BOLD correction is valid under the assumption that T_2^* contrast is the same in images with both contrasts, because they are acquired concomitantly (Huber et al., 2014). For each participant, we fit a voxel-wise general linear model restricted to the bilateral hMT+ ROI (previously defined) on both the BOLD and VASO time series in BrainVoyager. The model contained five predictors, one for each axis of motion condition and one for the flickering condition. Each predictor was then convolved with a standard hemodynamic response function. The GLM was corrected for temporal auto-correlation (AR2). Statistical t-maps were then computed. While generating the t-map by contrasting one axis of motion stimulus condition (e.g. horizontal) versus flickering dots baseline condition, the two contrasting conditions were balanced in terms of number of time points considered in the computation, since in the experimental paradigm the latter was repeated four times more than the former one. In addition to the t-maps, we also computed voxel-wise percent signal change (Huber et al., 2017; Beckett et al., 2020) between mean signal during task (e.g. moving dots along one axis of motion) and baseline (flickering dots) with the same balancing rationale used for computing t-maps. This method has been shown to provide results that are easier to interpret than methods using inferential statistics, which can be affected by laminar differences in noise and hemodynamic response function shape (Huber et al., 2017).

2.5.2. *Preference maps and tuning curves*

After the GLM fitting, we defined "tuned voxels" as all voxels that exhibited a significant t-value response (using a threshold (q) corrected for multiple comparisons using false discovery rate; q(FDR)<.05) when contrasting "all axes of motion moving dots vs flickering dots" and survived to a cluster-size thresholding (threshold=4) (using `https://gist.github.com/ofgulban/27c4491592126dce37e97c578cbf307b`). The higher sensitivity of BOLD was used to define the initial set of tuned voxels (BOLD mask) that were used in the following analysis steps for both BOLD and VASO contrasts. Having the same number of voxels allowed a more straightforward comparison between the two contrasts. Then, a main "preference map" was created by assigning to each voxel the preferred axis of motion, based on the predictor showing the highest fit (among the four axes of motion), representing the highest stimulus-induced normalized fMRI response (t-value). We computed tuning curves for each axis of motion, by averaging t-values responses of all voxels sharing the same preferred axis of motion. This procedure was separately performed for each participant and for both BOLD and VASO contrast in both hemispheres. A leave-one-run-out cross-validation method was implemented to assess the robustness of voxel tuning properties (Zimmermann et al., 2011; Emmerling, 2016). Iteratively, we divided the available number of runs (learning set) into training set (average of all runs excluding the test run) and test set (left out run) and for each set we labeled voxels according to their preferred axis, by fitting a GLM as explained above. Within each fold of the cross-validation process, only voxels showing the same axis preference between training and test set were kept for the next step. Finally, we cross-validated the "main preference map" by removing all voxels whose labeled preferred axis did not match with the cross-validated predicted label. A global measure of tuning specificity index was also computed for each tuning curve, by calculating the ratio of the response for the labeled axis of motion divided by the average response towards all other axes of motion (De Martino et al., 2013).

2.5.3. *Voxel-wise sensitivity and specificity calculation*

To investigate the signal behavior and differences between BOLD and VASO contrast, we developed new voxel-wise measures of sensitivity and specificity. By coding the voxel response to each axis of motion with a t-value, a four entries t-value vector was associated to each voxel. Negative t-values were zeroed. Sensitivity was computed by calculating the Euclidean norm of t-values vector ($\overrightarrow{v}$) (Eq.1).

$$Sensitivity \stackrel{\text{def}}{=} \|\overrightarrow{v}\| \tag{1}$$

For each voxel, a normalized measure of specificity was derived by normalizing the dot product between the t-values vector (entries were in ascending order) ($\widehat{v}$) and a reference winning vector [0 0 0 1] ($\widehat{w}$). Since the ordering operation constrains the angle computation in the range 0-60° (in 4 dimensions), we scaled the computed angle by the maximum angle (θ_{max}). Finally, we defined "specificity" the additive inverse of the computed scaled angle (Eq. 2).

$$Specificity \stackrel{\text{def}}{=} 1 - \frac{\arccos(\widehat{v} \cdot \widehat{w})}{\theta_{max}} \tag{2}$$

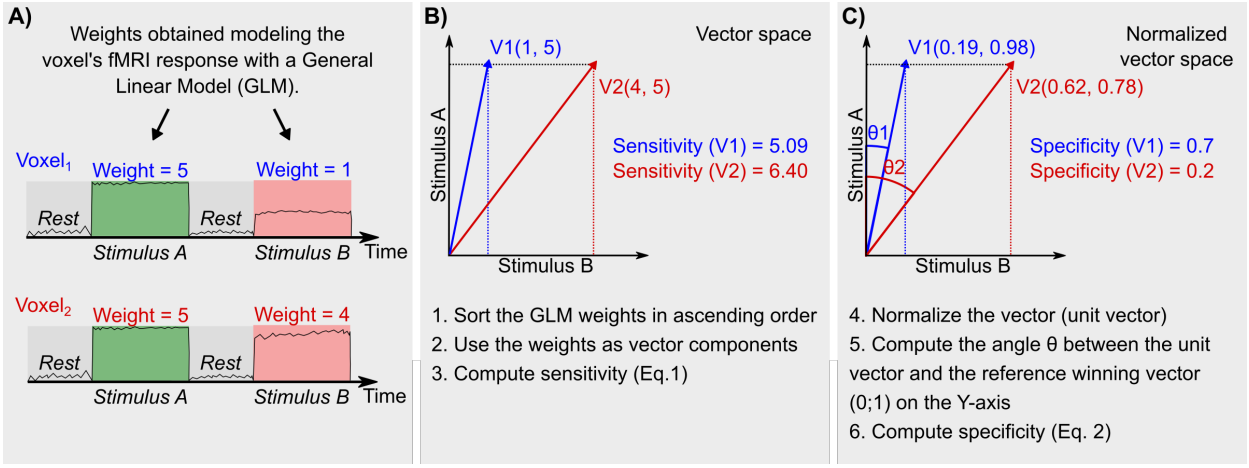

Figure 1: Numerical example of how to compute voxel-wise sensitivity and specificity for a 2 dimensional case. In A) the fMRI response of a voxel is modeled using a General Linear Model and the response modulation or "weight" (e.g. beta, t-value, percent signal change) during each stimulus is computed. In B) and C) we show step-by-step how to use the weights to compute our voxel-wise sensitivity and specificity.

In **Fig.1** we show with two numerical examples how to compute step-by-step our voxel-wise sensitivity and specificity measures. The sensitivity measure quantifies how strongly a voxel responds to any axis of motion. The specificity measure quantifies how well a voxel is tuned towards a specific axis of motion. We used a scatter plot to observe relationships between these two variables: different regions of the space were associated with different voxel's behavior (e.g. highly-tuned voxels or vessel-dominated voxels) (see **Fig.4A**). Furthermore, to detect and localize vessel-dominated voxels we combined sensitivity and specificity information with time-averaged T_2^*-weighted EPI intensity from BOLD time series, since it was demonstrated to be a robust marker of vascular effects (Kay et al., 2019). Alternative global measures of sensitivity and specificity were also implemented to compare our results to the literature (Beckett et al., 2020; Huber et al., 2017; Huber, 2017).

2.5.4. Voxel-wise columnarity index calculation

Cortical column detection and quantification using fMRI is a challenging task (Yacoub et al., 2008; Zimmermann et al., 2011; De Martino et al., 2015; Schneider et al., 2019). Inspired by Blazejewska et al. (2019), we implemented a searchlight-like algorithm to seek cylindrical columnar structures following the local coordinates of the cortical gray matter. This algorithm is implemented as a part of `LN2_UVD_FILTER` program (accessible via "-columns" option) in LayNii v2.2.1 and consists of the following steps:

1. Our primary inputs are the local coordinates of the cortical gray matter. These local coordinates consists of: (i) a voxel-wise parametrization of the cortical surface that contains the orthogonal U and V coordinates (computed by `LN2_MULTILATERATE` program), and (ii) voxel-wise equi-volume cortical depths that contains the D coordinates ("metric" file output as computed by `LN2_LAYERS` program) (see **Fig.2A**).

2. Our secondary input is a scalar map. This scalar map consists of the BOLD or VASO preference map (see **Fig.2B**).
3. Our tertiary input is a binary map which we refer to as "domain". This binary map consists of the initial set of tuned voxels (the "BOLD mask" used for both BOLD and VASO contrast, defined in the method section "Preference maps and tuning curves"). Note that we extended these activated voxels to cover the rest of the cortical thickness (using `LN2_UVD_FILTER` with "-max" option). For instance, if only a single middle gray matter voxel is available at a location, we include the voxels above and below until it covers the local cortical thickness.
4. The algorithm starts by evaluating a cylindrical 3D window centered at every voxel within the domain. This evaluation is done by (i) computing Euclidean distances using the UVD coordinates of the center voxel to all the other voxels within the domain, and (ii) by detecting the voxels that fall within user-determined radius and height of the cylinder. Note that we set the cylinder radius to 0.6 mm and the height to cover the full cortical depth (independent of a voxel being at the deep, middle, or superficial part of the cortex, see number I, II, III, IV in **Fig.2C**). We chose the diameter of the cylinder to be slightly higher than the nominal resolution (0.8 mm) in order to take into account all the possible orientations that a voxel can assume to sample the brain geometry.
5. This step determines a set of voxels for each window. Note that the number of windows is equal to the number of voxels within the domain input. However the total number of voxels for each window can change as a function of local cortical thickness and local curvature. Note that this behavior is natural and expected.
6. For the set of voxels within each window, we compute the modal (most frequently occurring) value within the BOLD or VASO preference maps.
7. Finally, we compute the "columnarity index" by dividing the number of voxels of the modal value with the total number of voxels evaluated in the cylindrical window (see **Fig.2D**). Note that the columnarity index ranges between 0 (no columnarity) to 1 (ideal or pure columnarity).

Upon completion, our algorithm yields a map where each voxel contains a unique columnarity index. This procedure allows us to reveal cortical columns for any value of the columnarity index by accordingly thresholding the columnarity map and applying it as a binary mask to the input preference map. We summarize the columnar behavior of hMT+ for both BOLD and VASO contrast by providing the following quantitative measurements as a function of the columnarity index: voxel-wise sensitivity and specificity (see **Fig.8A,B**) and percentage of columnar volume with respect to the volume of the domain (see **Fig.8C**). Finally, we evaluate the spatial similarity between BOLD and VASO columnarity maps by computing the spatial consistency: for each value of the columnarity index we quantify the percentage of voxels that appear in the same spatial location and with the same axis-of-motion preference in both contrasts with respect to the total amount of columnar voxels (see **Fig.8D**).

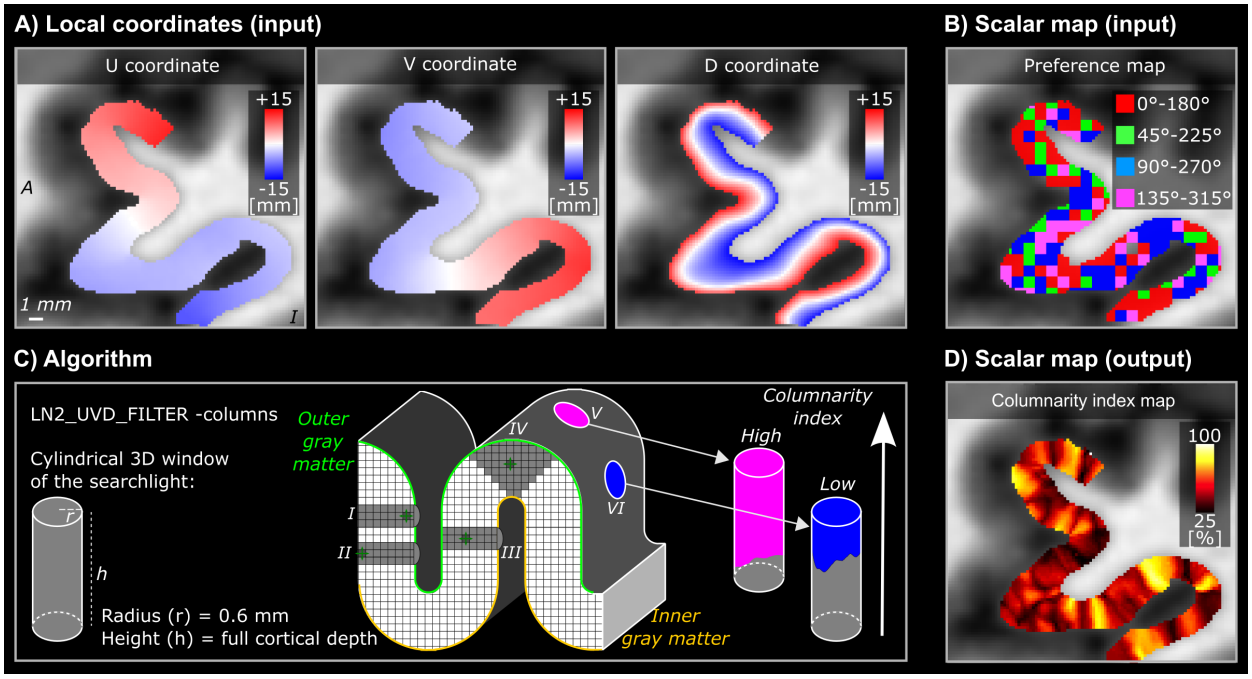

Figure 2: Overview of the searchlight algorithm for cortical column detection. A-B) Input examples of local coordinates (U, V, D) and BOLD preference map of left-hMT+ for one example participant (sub-01). C) Conceptualization of the algorithm on a toy model of a cortical ribbon. A searchlight with a cylindrical 3D window is evaluated at each voxel position. On the toy model, we show the searchlight (dark gray voxels with cardinal axes) and its relative 3D window (light gray). For every position of the searchlight, the window adapts to the geometry of the ribbon and covers the entire cortical depth (see examples (I) voxel close to the outer gray matter, (II) voxel close to the inner gray matter, (III) voxel close to the middle gray matter on a wall, (IV) voxel close to the middle gray matter on a gyrus). Pink cylinder is an example of a high columnarity index (V), whereas the blue cylinder is an example of a low columnarity index (VI). D) Output example of the columnarity index map generated for the data (B) of the same participant.

3. Results

3.1. Axes of motion tuning curves confirm motion-selective behavior

Participants performed well (97% accuracy) on the change detection task, indicating proper fixation throughout the experimental runs. For each participant, for both BOLD and VASO contrasts, we found voxels that exhibited a significant t-value response when contrasting "all axes of motion moving dots vs flickering dots" (see **Supplementary Fig.1**). As expected due to differences in sensitivity between BOLD and VASO contrast, the number of activated voxels for VASO was lower compared to BOLD when the same statistical threshold was used for both contrasts. The percentage of surviving cross-validated voxels for the left hMT+ was on average 35.8% for BOLD and 24.8% for VASO contrast across participants (S1 (38%, 25%); S2 (31%, 16%); S3 (39%, 25%); S4 (34%, 25%); S5 (37%, 33%)). The percentage of surviving cross-validated voxels for the right hMT+ was on average 37.6% for BOLD and 19.2% for VASO contrast across participants (S1 (39%, 16%); S2 (35%, 19%); S3 (40%, 24%); S4 (31%, 17%); S5 (43%, 20%)). We found axes of motion specific tuning curves for all cross-validated voxels in all participants for BOLD contrast in both hemispheres. This result confirms the previous fMRI results (Zimmermann et al., 2011; De Martino et al., 2013; Schneider et al., 2019). For the first time the results show that VASO is also sufficiently sensitive to map axes of motion in hMT+. Indeed, a characteristic peak at the preferred axis of motion is observed in each group of tuned voxels, showing a clear preference towards a single axis of motion (see **Fig.3** and **Supplementary Fig.2**). Despite the reduced signal sensitivity, the VASO tuning selectivity index was higher compared to BOLD (for VASO=4.8, for BOLD=1.7, on average across participants, conditions and hemispheres). Moreover, the percentage of cross-validated voxels for bilateral coverage across all participants characterizing each specific axis of motion was approximately uniform for BOLD (Horizontal 0°-180°: 27%, Vertical 90°-270°: 25%, Diagonal 45°-225°: 31%, Diagonal 135°-315°: 17%) and VASO (Horizontal 0°-180°: 24%, Vertical 90°-270°: 24%, Diagonal 45°-225°: 29%, Diagonal 135°-315°: 23%), without a clear bias towards any particular axis as previously observed by Albright (1984). See Supplementary **Supplementary Fig.3** as an example to compare tuning curves computed before and after the cross-validation process for the left-hMT+.

3.2. Voxel-wise sensitivity and specificity metrics quantify differences in imaging contrast

We computed voxel-wise sensitivity and specificity for all cross-validated tuned voxels for both BOLD and VASO contrast in both hemispheres. As observed in **Fig.4** and in **Supplementary Fig.4**, characteristic sensitivity-specificity scatter plots were found for both BOLD and VASO contrast. For all participants, we observed that BOLD cross-validated voxels are more sensitive (spanning a wider sensitivity range) and less specific (spanning a narrower specificity range) compared to VASO voxels. Despite its reduced signal sensitivity, VASO contrast provides greater specificity to microvasculature and less contributions from large vessels, in agreement with the higher functional tuning selectivity **Fig.3**.

Conventional layer profiles (**Supplementary Fig.5**) and global sensitivity and specificity measures were also computed (**Supplementary Fig.6**) to compare our results with the literature (Beckett et al., 2020; Huber et al., 2017).

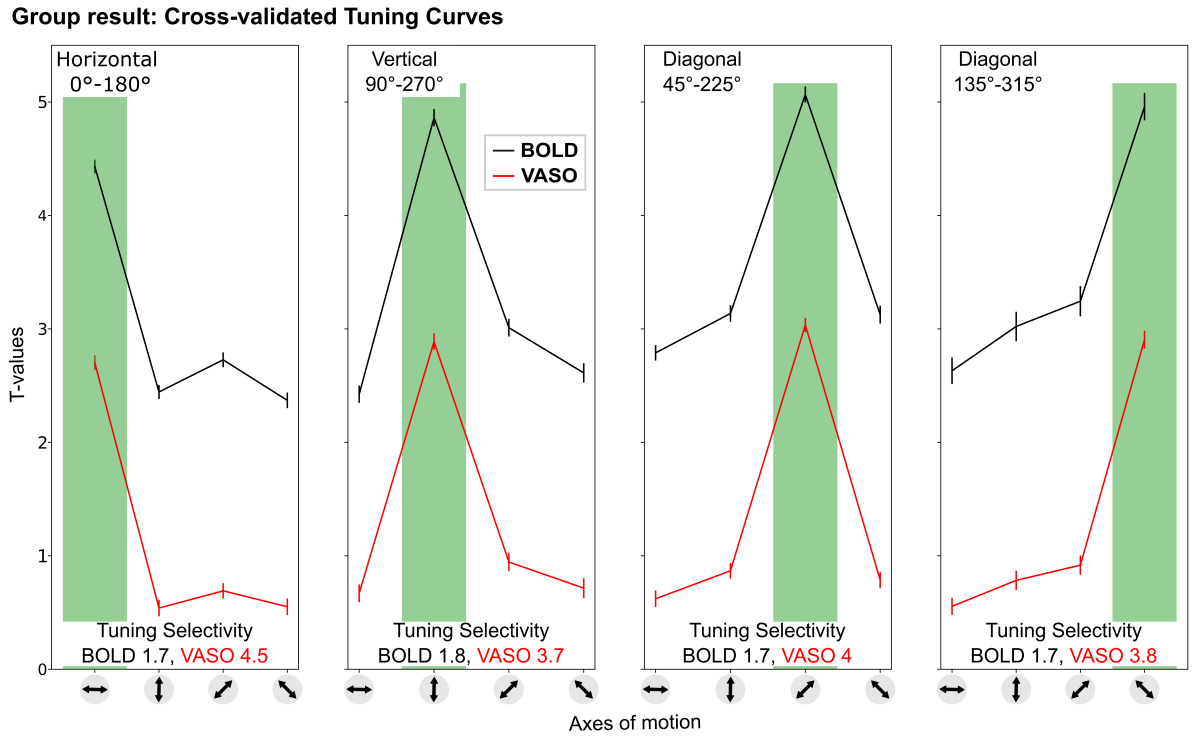

Figure 3: Group average axis of motion selectivity tuning curves for each axis of motion for both BOLD and VASO contrast in the left hMT+. Tuning curves are computed by averaging t-values of all cross-validated (leave-one-run-out approach) voxels sharing the same preferred axis of motion. The plots depict the mean and the standard error of all voxels for each category. Tuning selectivity index is reported on the bottom of each subplot for both BOLD and VASO contrast (colors refer to the legend reported in the second column). Consistently, the VASO tuning selectivity index is higher than the BOLD. Cross validated tuning curves for the right hMT+ are shown in **Supplementary Fig.2**

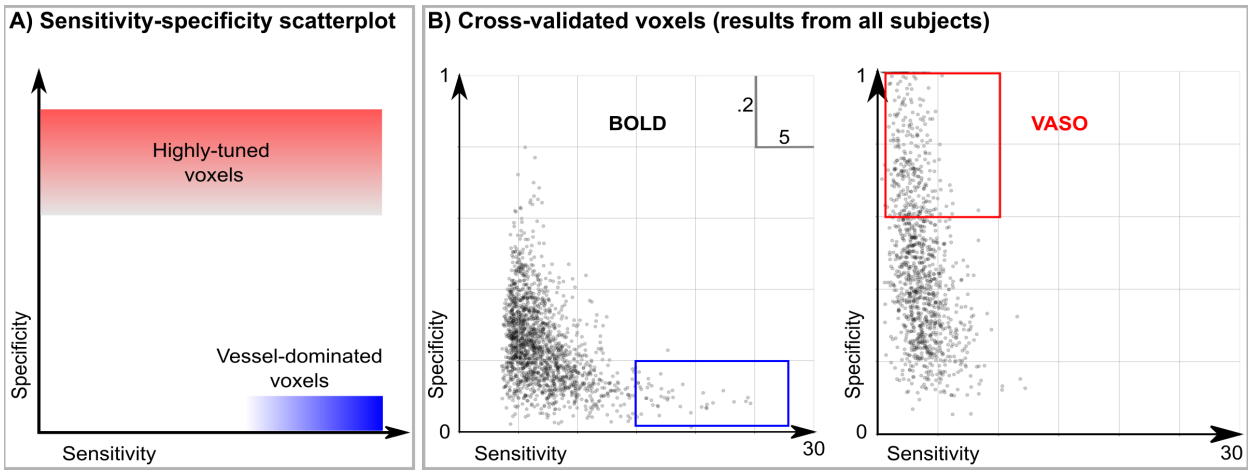

Figure 4: A) Sensitivity-specificity scatter plot. Different regions of the space are associated with different voxel characteristics. The red area refers to highly tuned voxels, whereas the blue area describes vessel-dominated voxels. B) Sensitivity and specificity quantify cross-validated voxel behavior of all participants for both BOLD and VASO contrast. Squares highlight main differences between contrast types. In this figure, voxels belong to the left hMT+. Consistently, voxels belonging to the right hMT+ show the same behavior (see **Supplementary Fig.4**).

Both supplementary results are in agreement with results in **Fig.4**. Our new local sensitivity and specificity measures offer a voxel-wise perspective on the draining veins effect: the vessel-dominated voxels responsible for this effect can be straightforwardly detected and localized.

As shown for an exemplary participant in **Fig.5**, the combination of high sensitivity and low specificity help detecting vessel-dominated voxels (highlighted by green arrows) similarly to decreased BOLD T_2^*-weighted EPI intensity that has been shown to be a robust marker of vascular effects (Kay et al., 2019). A lower number of vessel-dominated voxels are found for VASO contrast compared to BOLD, demonstrating the reduced signal contamination by draining veins and its improved specificity.

In **Fig.6**, we project the vessels-dominated voxels shown in **Fig.5** in the flat laminar-resolved domain. This representation provides a more convenient visual representation to evaluate voxel localization across cortical depths. As shown in **Fig.6**, the vessels-dominated voxels appear mostly in the superficial layers and disappear in the deep layers. This result demonstrates BOLD signal contamination by pial vasculature that lies above the cortex. The same phenomenon is strongly attenuated in VASO signals.

3.3. Quantification of the columnar organization of axes of motion tuned voxels

We explored the spatial organization of axes of motion tuned voxels for both BOLD and VASO contrast by using a new searchlight-style algorithm for column detection. We evaluated both BOLD and VASO columnarity maps for 25%, 50%, and 65% of the columnarity index in left hMT+ ROI. We used the flattening algorithm (Gulban et al., 2021) and 3D rendering visualization tools (Sullivan and Kaszynski, 2019) to show our columnar results.

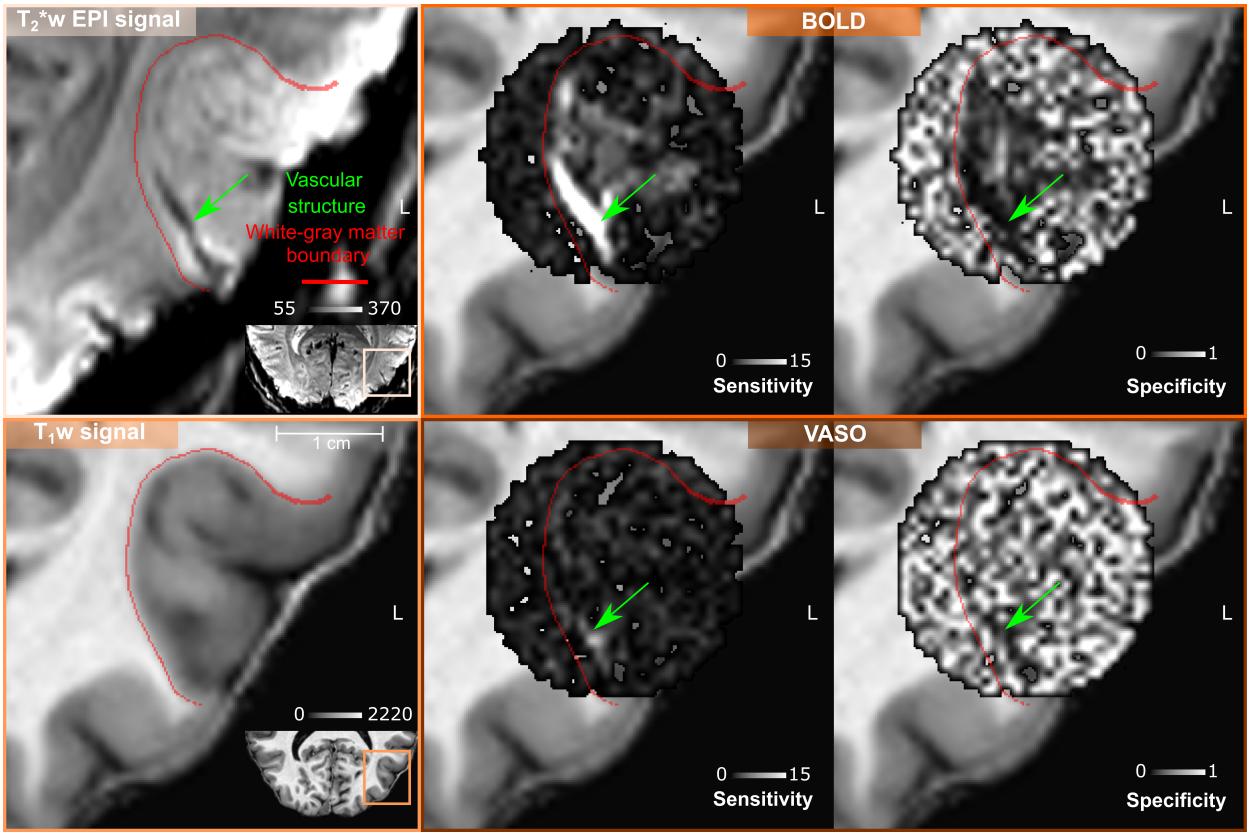

Figure 5: Volume-based visualization of voxel-wise sensitivity and specificity maps for one example participant (sub-01) in the left hMT+ ROI. The same axial slice is shown for both T_2^*-w EPI signal and T_1-w signal (nominal resolution 0.2 iso mm). The green arrow points to a vascular structure detectable only through T_2^*-w EPI intensity as a dark spot (reflecting static susceptibility effects). High sensitivity and low specificity characterizes all the voxels belonging to this vascular structure (green arrows) for BOLD contrast. The detectability of this vascular structure is less evident for VASO contrast, as expected.

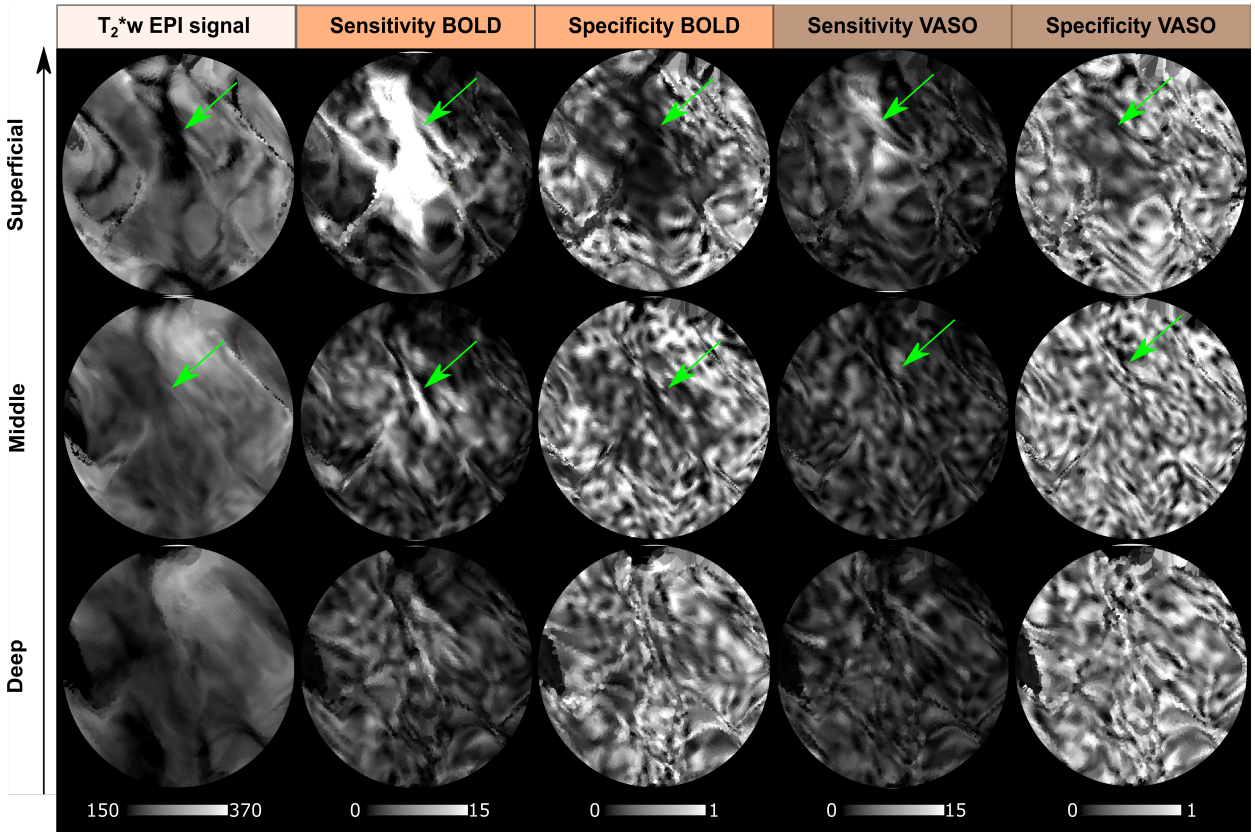

Figure 6: Depth-dependent T_2^*-w EPI intensity, voxel-wise sensitivity and specificity maps for BOLD and VASO contrast showed for the flattened left hMT+ ROI for one example participant (sub-01) (nominal resolution 0.05 mm iso.). Note that in this figure we project the same vessels-dominated voxels shown in **Fig.5** in the flat laminar-resolved domain. The vascular structure highlighted by the green arrow corresponding to the dark spot in T_2^*-w EPI intensity is clearly visible at superficial layers but not at middle or deep layers, which indicates that it is a pial vein. High sensitivity and low specificity are in agreement with the spatial displacement of darkness of T_2^*-w EPI intensity.

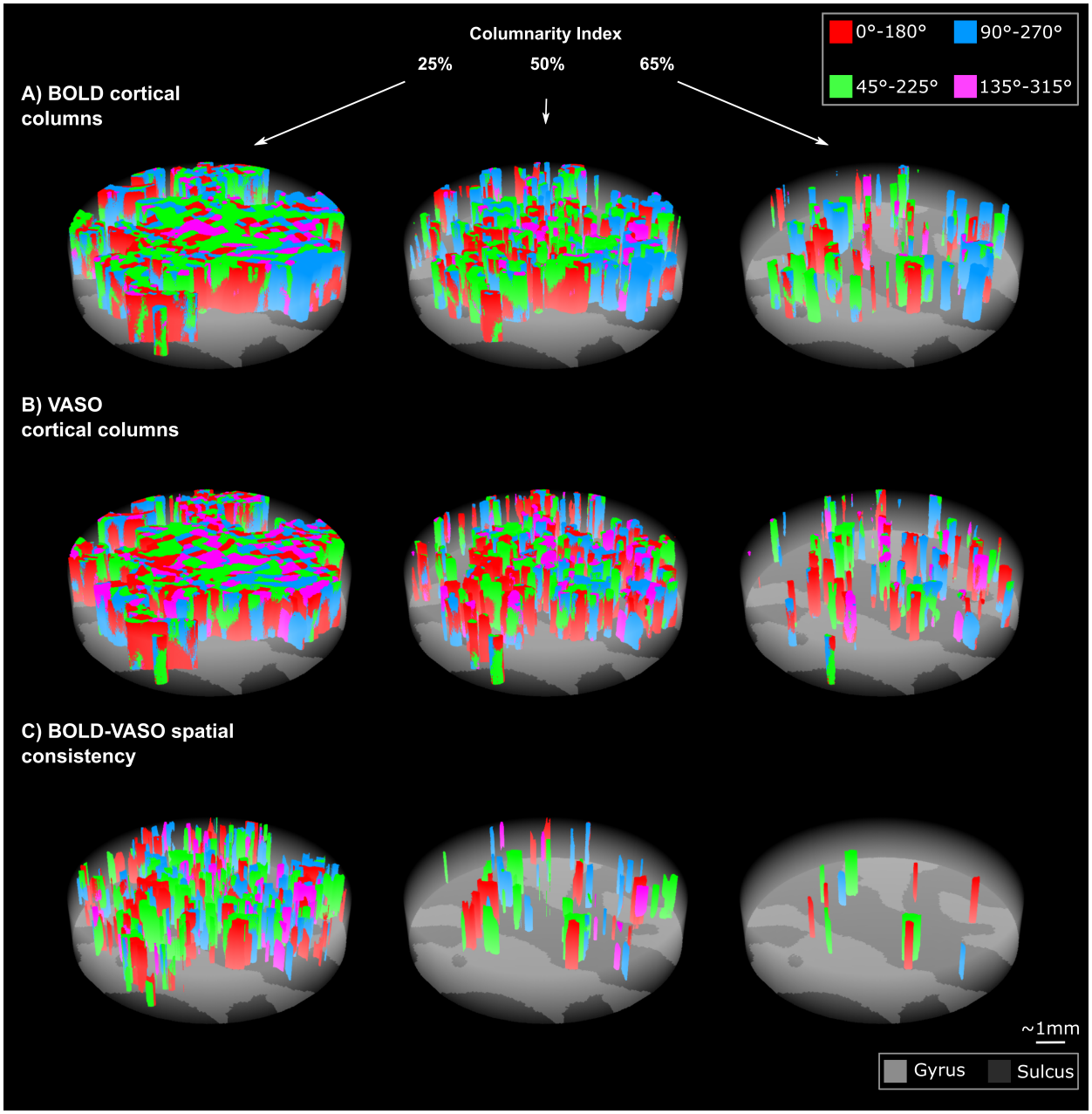

Figure 7: Examples of BOLD (A) and VASO (B) axes of motion cortical columns for one example participant (sub-01) at 25%, 50%, 65% of the columnarity index. C) BOLD-VASO spatial consistency shows only axes of motion columns that are detected in both BOLD and VASO contrasts for each columnarity threshold (see animations here: `https://doi.org/10.6084/m9.figshare.20393667`.

In particular, **Fig.7A,B** shows BOLD and VASO columnar results for one representative participant. We further emphasized the visualization of our columnar results by creating rotating animations available here: `https://doi.org/10.6084/m9.figshare.20393667`. We found that the animations allowed us to qualitatively communicate the spatial organization of our volume of interest in an effective way. For each participant and for both BOLD and VASO we quantified four features as a function of the columnarity index: the amount of spatial overlap or consistency between BOLD and VASO columnar results, the local sensitivity and specificity and the columnar volume. **Fig.7C** shows BOLD-VASO spatial consistency for the same three columnarity indices (25%, 50%, 65%).

As it can be seen in the group results of **Fig.8D** the BOLD-VASO spatial consistency decreases as the columnarity index increases. The same trend is also found for the columnarity volume (**Fig.8C**). Despite the higher sensitivity of the BOLD columnarity results compared to VASO (**Fig.8A**), interestingly, we found that VASO columnarity results are always more specific according to our local measure of specificity compared to BOLD results (**Fig.8B**).

4. Discussion

4.1. Overview of the results

This study shows for the first time the feasibility of mapping axes of motion cortical columns in the extrastriate area hMT+ in living humans using CBV-VASO fMRI at 7T. The SS-SI VASO sequence with 3D EPI readout enabled us to simultaneously acquire BOLD and VASO responses in hMT+. Therefore, we separately applied the same analysis pipeline to both VASO and BOLD fMRI data (Huber et al., 2015, 2017; Oliveira et al., 2022; Oliveira et al.). In this regard, the development of new local metrics of sensitivity and specificity was pivotal to quantitatively compare and interpret results found with VASO and BOLD contrast. Our metrics not only confirmed the higher specificity and lower sensitivity of VASO compared to BOLD voxels (Beckett et al., 2020), but also allowed us to clearly highlight pial vein effects in BOLD contrast. Finally, the new searchlight algorithm for functional column detection provides a unique framework to investigate mesoscopic cortical features with its improved quantifiability and comparability with respect to previous used methodologies (Yacoub et al., 2008; Zimmermann et al., 2011; De Martino et al., 2013, 2015; Schneider et al., 2019). The columnarity map computed by our algorithm provides a full representation of the 3D functional organization of hMT+ allowing a transparent evaluation of columnarity.

4.1.1. Local vs global sensitivity and specificity metrics

Conventionally, global measures of sensitivity and specificity (Huber et al., 2017; Beckett et al., 2020) are used to compare different contrast mechanisms in terms of draining veins effects. As described in (Beckett et al., 2020) those global indices are computed by fitting a linear regression model to layer profiles (see Supplementary **Fig.6**). In this work, we extended the concept of sensitivity and specificity from a global to a voxel-wise scale, by exploiting the tuning property of hMT+ voxels. By visualizing our sensitivity and specificity maps, we observed that untuned voxels show very low specificity. Voxels close to pial vessels show a very low specificity and very high sensitivity in

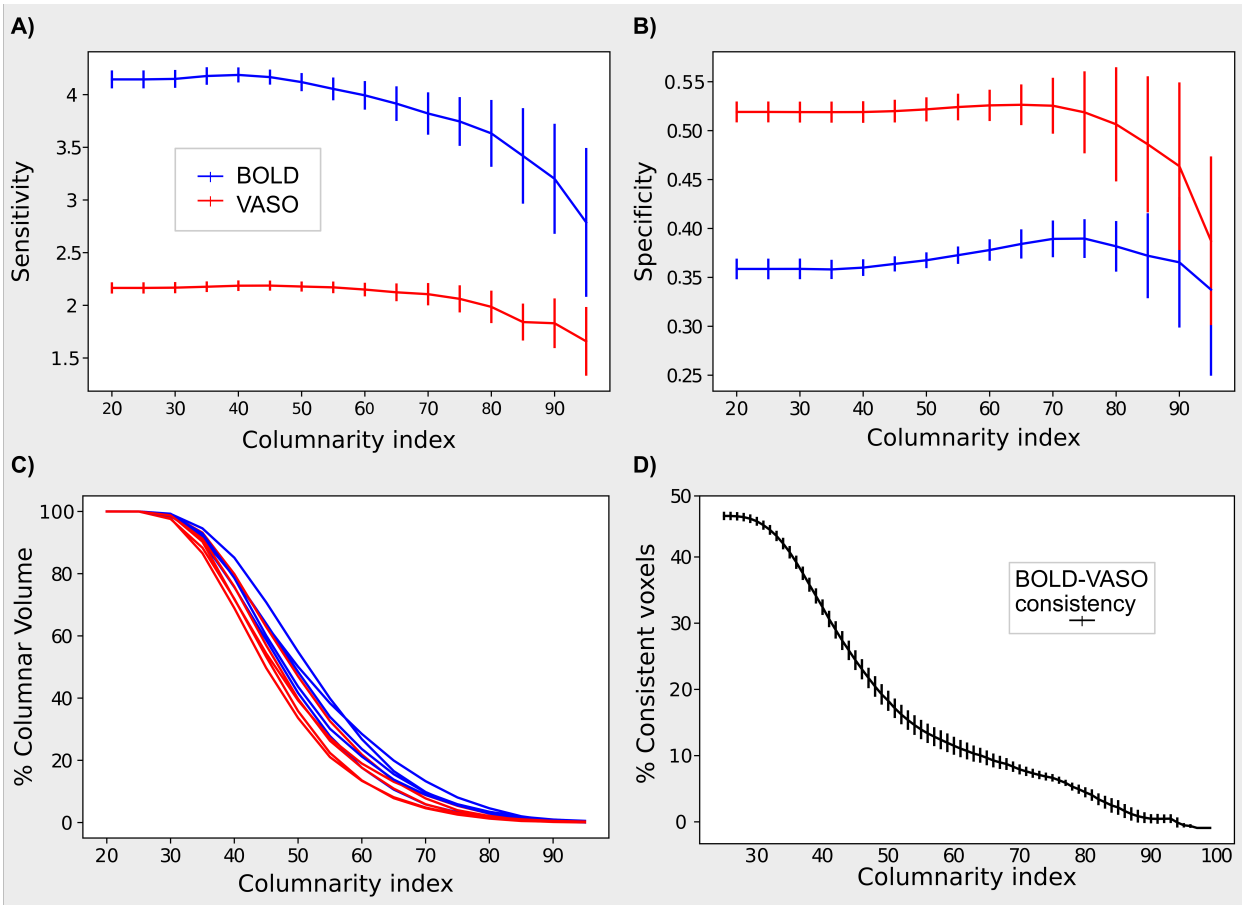

Figure 8: Descriptive statistics for columnarity group results for the left hMT+ ROI. A-B) Voxel-wise sensitivity and specificity is evaluated for both BOLD (blue line) and VASO (red line) as a function of the columnarity index. Line plot represents the mean specificity computed across participants. Error bar represents the standard error across participants. C) The percentage of columnarity volume is evaluated as a function of the columnarity index for both BOLD and VASO contrast. Each line is representative of one participant. D) BOLD-VASO spatial consistency quantified for each value of the columnarity index. Line plot represents the averaged BOLD-VASO spatial consistency computed across participants and error bar represents the standard error across participants.

combination with a low T_2^*-w EPI signal as an additional independent diagnostic marker. For the data of the participant reported in **Fig.5** and in **Fig.6**, we clearly showed BOLD voxels sampling a pial vessel. The VASO contrast is expected to be not sensitive to macrovasculature. However, we still observe a smaller number of voxels with the aforementioned properties. Two possible candidate mechanisms can be leading to this phenomenon: a flow-dependent vein effect as described in (Huber, 2015) or a dilatation effect of big arteries on the pial surface (Kim et al., 2013), which is still disputed. We believe that our new local metrics of sensitivity and specificity provide an alternative way to evaluate the draining veins effect and to visualize pial vessels responsible for it.

4.1.2. General perspective on cortical columns

While the existence of direction selective neurons within area MT is a well-established feature in primates (Albright, 1984) and cats (Hubel and Wiesel, 1962, 1965) only preliminary evidence has been reported in humans (Zimmermann et al., 2011; De Martino et al., 2013). Our findings provide strong evidence for a functional columnar organization of axis-of-motion features also in human MT+. The obtained columnarity maps, however, indicate that functional clusters are only partially in line with proposed ideal (anatomical) column models (Mountcastle, 1956) that are assumed to penetrate vertically from the pial surface to the white matter boundary in a regular manner. The hypothesis of 3D columns was mostly investigated by multi-unit electrophysiological recordings in animals. Pioneering results from Hubel and Wiesel (1962, 1965); Albright et al. (1984), were put in perspective by reports showing that the preferred orientations were not necessarily represented in a columnar fashion in animal visual cortex (Bauer et al., 1983, 1989; Berman et al., 1987). In particular, Bauer et al. (1983) reported that the preferred orientations jump by 90° along the vertical track of the electrode penetration in the cat area 18. It's worth noting that this technique comes with the cumbersome task of accurately tracing the penetrating electrodes together with the limited sampling space, affecting the robustness of those results (Horton and Adams, 2005). Later findings (Tanaka et al., 2011) provided a new perspective on the conventional columnar view of orientation representation of the visual cortex: simulations based on a 3D self-organized model predicted the occurrence of direction reversal in columns along the cortical depth dimension being proportional to the curvature of the cortex, and orientation columns having wedge-like shape when sampling gyri or sulci. The same study confirmed these theoretical predictions with multi-slice, high-resolution functional MRI in cat areas 17 and 18. These mechanisms were also discussed by (Zimmermann et al., 2011) to explain the variability of iso-oriented feature maps across cortical depths observed with high-resolution fMRI in humans. Recently, Nakamichi et al. (2018) proposed a new explanation for the variability across cortical depths based on functional optical coherence tomography in cats: their results show that the 3D structure of orientation columns were heavily distorted around pinwheel centers. Orientation singularities were rarely straight solid bars connecting pinwheel centers, instead they typically ran inside the cortex creating "singularity strings" with peculiar trajectories. Besides findings challenging a simplistic view of columnar organization (Rakic, 2008), the functional relevance of cortical columns has also been debated (Horton and Adams, 2005; Haueis, 2021). Whether cortical columns "are a structure without a function" (Horton and Adams, 2005) or not, the presence of functional clusters with groups of neurons that share similar tuning

properties allows high-resolution human fMRI studies to reveal coding principles of the brain, which would otherwise only be possible at microscopic resolution.

Our columnar results are to our knowledge the first to provide a quantitative columnarity map to characterize the functional organization of axis-of-motion features in hMT+ exploiting the benefits of CBV-based fMRI at 7T. Our new algorithm for column detection not only improved the quantifiability and comparability with other studies, but it also takes into account the curvature effect (Tanaka et al., 2011). However, we found that the spatial consistency between VASO and BOLD columnar results decreased as a function of the columnarity index. We believe that this variability is due to an interplay of two effects. On the one hand, the differences in terms of sensitivity but especially specificity between VASO and BOLD would mostly affect the columnar results when a conservative columnarity index threshold is applied. On the other hand, the aforementioned theory of variability of orientation selectivity across cortical depths could explain the trend of spatial consistency.

Future CBV-sensitive fMRI studies with higher spatial resolution (e.g. < 0.5 mm isotropic) and improved sensitivity would be able to investigate the functional organization of hMT+ in more detail that would be likely sufficient to resolve direction-of-motion columns instead of the larger axis-of-motion columns. Such higher-resolution fMRI studies might also reveal direct evidence for pinwheels and their effect on columnarity. The improved quantifiability provided by our new method for column detection will make the comparison of our results with future studies straightforward.

Data and code availability statement

Analysis code is available on github: `https://github.com/27-apizzuti/AOM-VASO_project`. Data will be made available upon manuscript acceptance.

Author Contributions

According to the CRediT system (https://casrai.org/credit/)

Conceptualization: A.P., R.H., O.F.G., R.G.

Methodology: A.P., O.F.G., J.P., R.G.

Software: A.P., O.F.G.

Validation: A.P., R.H., O.F.G., R.G.

Formal Analysis: A.P.

Investigation: A.P., R.H., A.B.A.

Resources: A.P., R.H., O.F.G., A.B.A., J.P., R.G.

Data curation: A.P., A.B.A.

Writing – original draft: A.P.

Writing – review & editing: A.P., R.H., O.F.G., A.B.A., J.P., R.G.

Visualization: A.P., R.H., O.F.G., R.G.

Supervision: R.H., O.F.G., J.P., R.G.

Project administration: R.H., J.P., R.G.

Funding acquisition: R.G.

Acknowledgements

This project was funded by the EU-project H2020-860563 euSNN and the European Union's Horizon 2020 Framework Programme for Research and Innovation under the Specific Grant Agreement No. 945539 (Human Brain Project SGA3). Laurentius Huber was funded from the NWO VENI project 016.Veni.198.032. The sequence used here is based on code kindly written and provided by Benedikt A. Poser. Data was acquired at Scannexus (Maastricht, the Netherlands). We thank Chris Wiggins for providing the 3rd order shimming tools. We thank David Feinburg for valuable discussions on the columnar results. We would also like to thank *Maastricht Layer-Seminar* members Sebastian Dresbach, Lonike Faes, Miriam Heynckes, Kenshu Koiso, and Yawen Wang for discussions throughout the project.

References

Albright, T.D., 1984. Direction and orientation selectivity of neurons in visual area MT of the macaque. Journal of Neurophysiology 52, 1106–1130. doi:10.1152/jn.1984.52.6.1106.

Albright, T.D., Desimone, R., Gross, C.G., 1984. Columnar organization of directionally selective cells in visual area MT of the Macaque. Journal of Neurophysiology 51, 16–31. doi:10.1152/jn.1984.51.1.16.

Ashburner, J., Friston, K.J., 2005. Unified segmentation. NeuroImage 26, 839–851. doi:10.1016/j.neuroimage.2005.02.018.

Avants, B.B., Tustison, N., Song, G., others, 2009. Advanced normalization tools (ANTS). Insight j 2, 1–35.

Avants, B.B., Tustison, N.J., Song, G., Cook, P.A., Klein, A., Gee, J.C., 2011. A reproducible evaluation of ANTs similarity metric performance in brain image registration. NeuroImage 54, 2033–2044. URL: http://dx.doi.org/10.1016/j.neuroimage.2010.09.025, doi:10.1016/j.neuroimage.2010.09.025.

Bauer, R., Dow, B.M., Snyder, A.Z., Vautin, R., 1983. Orientation shift between upper and lower layers in monkey visual cortex. Experimental Brain Research 50, 133–145. doi:10.1007/BF00238240.

Bauer, R., Eckhorn, R., Jordan, W., 1989. Iso- and cross-oriented columns in cat striate cortex: A study with simultaneous single- and multi-unit recordings. Neuroscience 30, 733–740. doi:10.1016/0306-4522(89)90165-6.

Beckett, A.J., Dadakova, T., Townsend, J., Huber, L., Park, S., Feinberg, D.A., 2020. Comparison of BOLD and CBV using 3D EPI and 3D GRASE for cortical layer functional MRI at 7 T. Magnetic Resonance in Medicine 84, 3128–3145. doi:10.1002/mrm.28347.

Berman, N.E., Wilkes, M.E., Payne, B.R., 1987. Organization of orientation and direction selectivity in areas 17 and 18 of cat cerebral cortex. Journal of Neurophysiology 58, 676–699. doi:10.1152/jn.1987.58.4.676.

Blazejewska, A.I., Fischl, B., Wald, L.L., Polimeni, J.R., 2019. Intracortical smoothing of small-voxel fMRI data can provide increased detection power without spatial resolution losses compared to conventional large-voxel fMRI data. NeuroImage 189, 601–614. URL: https://doi.org/10.1016/j.neuroimage.2019.01.054, doi:10.1016/j.neuroimage.2019.01.054.

Bok, S.T., 1959. Histonomy of the Cerebral Cortex. Elsevier.

Born, R.T., Bradley, D.C., 2005. Structure and function of visual area MT. Annual Review of Neuroscience 28, 157–189. doi:10.1146/annurev.neuro.26.041002.131052.

Breman, H., Mulders, J., Fritz, L., Peters, J., Pyles, J., Eck, J., Bastiani, M., Roebroeck, A., Ashburner, J., Goebel, R., 2020. An image registration-based method for epi distortion correction based on opposite phase encoding (COPE), in: Lecture Notes in Computer Science (including subseries Lecture Notes in Artificial Intelligence and Lecture Notes in Bioinformatics), Springer. pp. 122–130. doi:10.1007/978-3-030-50120-4{_}12.

Buxhoeveden, D.P., Casanova, M.F., 2002. The minicolumn hypothesis in neuroscience. Brain 125, 935–951. doi:10.1093/brain/awf110.

Cho, S., Roy, A., Liu, C.J., Idiyatullin, D., Zhu, W., Zhang, Y., Zhu, X.H., O'Herron, P., Leikvoll, A., Chen, W., Kara, P., Uğurbil, K., 2022. Cortical layer-specific differences in stimulus selectivity revealed with high-field fMRI and single-vessel resolution optical imaging of the primary visual cortex. NeuroImage 251. doi:10.1016/j.neuroimage.2022.118978.

Cox, R.W., 1996. AFNI: Software for analysis and visualization of functional magnetic resonance neuroimages 29, 162–173. URL: https://linkinghub.elsevier.com/retrieve/pii/S0010480996900142, doi:10.1006/cbmr.1996.0014.

Cox, R.W., Hyde, J.S., 1997. Software Tools for Analysis and Visualization of FMRI Data NMR in Biomedicine, in press. NMR Biomed 10, 171–8. URL: https://afni.nimh.nih.gov/pub/dist/doc/papers/afni_paper2.pdf.

De Martino, F., Moerel, M., Ugurbil, K., Goebel, R., Yacoub, E., Formisano, E., 2015. Frequency preference and attention effects across cortical depths in the human primary auditory cortex. Proceedings of the National Academy of Sciences of the United States of America 112, 16036–16041. doi:10.1073/pnas.1507552112.

De Martino, F., Yacoub, E., Kemper, V., Moerel, M., Uludag, K., De Weerd, P., Ugurbil, K., Goebel, R., Formisano, E., 2018. The impact of ultra-high field MRI on cognitive and computational neuroimaging. NeuroImage 168, 366–382. doi:10.1016/j.neuroimage.2017.03.060.

De Martino, F., Zimmermann, J., Muckli, L., Ugurbil, K., Yacoub, E., Goebel, R., 2013. Cortical Depth Dependent Functional Responses in Humans at 7T: Improved Specificity with 3D GRASE. PLoS ONE 8. doi:10.1371/journal.pone.0060514.

Diogo, A.C.M., Soares, J.G., Koulakov, A., Albright, T.D., Gattass, R., 2003. Electrophysiological imaging of functional architecture in the cortical middle temporal visual area of Cebus apella monkey. Journal of Neuroscience 23, 3881–3898. doi:10.1523/jneurosci.23-09-03881.2003.

Dumoulin, S.O., Fracasso, A., van der Zwaag, W., Siero, J.C., Petridou, N., 2018. Ultra-high field MRI: Advancing systems neuroscience towards mesoscopic human brain function. NeuroImage 168, 345–357. URL: https://doi.org/10.1016/j.neuroimage.2017.01.028, doi:10.1016/j.neuroimage.2017.01.028.

Duvernoy, H.M., Delon, S., Vannson, J.L., 1981. Cortical blood vessels of the human brain. Brain Research Bulletin 7, 519–579. doi:10.1016/0361-9230(81)90007-1.

Emmerling, T.C., 2016. Imaging imagery. Ph.D. thesis. maastricht university. URL: https://cris.maastrichtuniversity.nl/en/publications/85216681-d6a8-4898-beec-645b255b9c43, doi:10.26481/dis.20160622te.

Feinberg, D.A., Kiefer, B., Johnson, G., 1995. GRASE Improves Spatial Resolution in Single Shot Imaging. Magnetic Resonance in Medicine 33, 529–533. doi:10.1002/mrm.1910330411.

Friston, K.J., Ashburner, J.T., Kiebel, S.J., Nichols, T.E., Penny, W.D., 2007. Statistical Parametric Mapping: The Analysis of Functional Brain Images. volume 8. URL: http://books.elsevier.com/neuro/?isbn=9780123725608&srccode=89660.

Glover, G.H., Li, T.q., Ress, D., 2000. Image-based method for retrospective correction of physiological motion effects in fMRI: RETROICOR. Magnetic Resonance in Medicine 44, 162–167. doi:10.1002/1522-2594(200007)44:1<162::aid-mrm23>3.3.co;2-5.

Goebel, R., Khorram-Sefat, D., Muckli, L., Hacker, H., Singer, W., 1998. The constructive nature of vision: Direct evidence from functional magnetic resonance imaging studies of apparent motion and motion imagery. European Journal of Neuroscience 10, 1563–1573. doi:10.1046/j.1460-9568.1998.00181.x.

Goebel, R., Muckli, L., Kim, D.S., 2012. Visual System. The Human Nervous System , 1301–1327doi:10.1016/B978-0-12-374236-0.10037-9.

Guidi, M., Huber, L., Lampe, L., Merola, A., Ihle, K., Möller, H.E., 2020. Cortical laminar resting-state signal fluctuations scale with the hypercapnic blood oxygenation level-dependent response. Human Brain Mapping 41, 2014–2027. doi:10.1002/hbm.24926.

Gulban, O.F., Bollmann, S., Huber, R., Wagstyl, K., Goebel, R., Poser, B.A., Kay, K., Ivanov, D., 2021. Mesoscopic Quantification of Cortical Architecture in the Living Human Brain. bioRxiv , 1–23URL: https://www.biorxiv.org/content/10.1101/2021.11.25.470023, doi:10.1101/2021.11.25.470023.

Gulban, O.F., Schneider, M., Marquardt, I., Haast, R.A., De Martino, F., 2018. A scalable method to improve gray matter segmentation at ultra high field MRI. PLoS ONE 13, 1–31. doi:10.1371/journal.pone.0198335.

Haueis, P., 2021. The death of the cortical column? Patchwork structure and conceptual retirement in neuroscientific practice. Studies in History and Philosophy of Science 85, 101–113. URL: https://doi.org/10.1016/j.shpsa.2020.09.010, doi:10.1016/j.shpsa.2020.09.010.

Horton, J.G., Adams, D.L., 2005. The cortical column: A structure without a function. Philosophical Transactions of the Royal Society B: Biological Sciences 360, 837–862. doi:10.1098/rstb.2005.1623.

Hua, J., Jones, C.K., Qin, Q., Van Zijl, P.C., 2013. Implementation of vascular-space-occupancy MRI at 7T. Magnetic Resonance in Medicine 69, 1003–1013. doi:10.1002/mrm.24334.

Hubel, D.H., Wiesel, T.N., 1962. Receptive fields, binocular interaction and functional architecture in the cat's visual cortex. The Journal of Physiology 160, 106–154. URL: https://onlinelibrary.wiley.com/doi/10.1113/jphysiol.1962.sp006837, doi:10.1113/jphysiol.1962.sp006837.

Hubel, D.H., Wiesel, T.N., 1965. Receptive fields and functional architecture in two nonstriate visual areas (18 and 19) of the cat. Journal of Neurophysiology 28, 229–289. URL: http://www.ncbi.nlm.nih.gov/pubmed/14283058http://www.physiology.org/doi/10.1152/jn.1965.28.2.229, doi:10.1152/jn.1965.28.2.229.

Huber, L., 2015. Mapping human brain activity by functional magnetic resonance imaging of blood volume. Ph.D. thesis. URL: http://nbn-resolving.de/urn:nbn:de:bsz:15-qucosa-165252.

Huber, L., Finn, E.S., Chai, Y., Goebel, R., Stirnberg, R., Stöcker, T., Marrett, S., Uludag, K., Kim, S.G., Han, S.H., Bandettini, P.A., Poser, B.A., 2020. Layer-dependent functional connectivity methods. URL: https://doi.org/10.1016/j.pneurobio.2020.101835, doi:10.1016/j.pneurobio.2020.101835.

Huber, L., Goense, J., Kennerley, A.J., Trampel, R., Guidi, M., Reimer, E., Ivanov, D., Neef, N., Gauthier, C.J., Turner, R., Möller, H.E., 2015. Cortical lamina-dependent blood volume changes in human brain at 7T. NeuroImage 107, 23–33. URL: http://dx.doi.org/10.1016/j.neuroimage.2014.11.046, doi:10.1016/j.neuroimage.2014.11.046.

Huber, L., Handwerker, D.A., Jangraw, D.C., Chen, G., Hall, A., Stüber, C., Gonzalez-Castillo, J., Ivanov, D., Marrett, S., Guidi, M., Goense, J., Poser, B.A., Bandettini, P.A., 2017. High-Resolution CBV-fMRI Allows Mapping of Laminar Activity and Connectivity of Cortical Input and Output in Human M1. Neuron 96, 1253–1263. doi:10.1016/j.neuron.2017.11.005.

Huber, L., Ivanov, D., Handwerker, D.A., Marrett, S., Guidi, M., Uludağ, K., Bandettini, P.A., Poser, B.A., 2018. Techniques for blood volume fMRI with VASO: From low-resolution mapping towards sub-millimeter layer-dependent applications. NeuroImage 164, 131–143. doi:10.1016/j.neuroimage.2016.11.039.

Huber, L., Ivanov, D., Krieger, S.N., Streicher, M.N., Mildner, T., Poser, B.A., Möller, H.E., Turner, R., 2014. Slab-selective, BOLD-corrected VASO at 7 tesla provides measures of cerebral blood volume reactivity with high signal-to-noise ratio. Magnetic Resonance in Medicine 72, 137–148. doi:10.1002/mrm.24916.

Huber, L.R., Poser, B.A., Bandettini, P.A., Arora, K., Wagstyl, K., Cho, S., Goense, J., Nothnagel, N., Morgan, A.T., van den Hurk, J., Müller, A.K., Reynolds, R.C., Glen, D.R., Goebel, R., Gulban, O.F., 2021. LayNii: A software suite for layer-fMRI. NeuroImage 237, 118091. URL: https://doi.org/10.1016/j.neuroimage.2021.118091, doi:10.1016/j.neuroimage.2021.118091.

Huber, L.R.R., 2017. Which fMRI contrast is most specific for high resolution layer-dependent fMRI? Comparison study of GE-BOLD, SE-BOLD, T2-prep BOLD and blood volume fMRI.

Huk, A.C., Dougherty, R.F., Heeger, D.J., 2002. Retinotopy and functional subdivision of human areas MT and MST. Journal of Neuroscience 22, 7195–7205. URL: https://www.jneurosci.org/lookup/doi/10.1523/JNEUROSCI.22-16-07195.2002, doi:10.1523/jneurosci.22-16-07195.2002.

Kay, K., Jamison, K.W., Vizioli, L., Zhang, R., Margalit, E., Ugurbil, K., 2019. A critical assessment of data quality and venous effects in sub-millimeter fMRI. NeuroImage 189, 847–869. URL: https://doi.org/10.1016/j.neuroimage.2019.02.006, doi:10.1016/j.neuroimage.2019.02.006.

Kemper, V.G., De Martino, F., Vu, A.T., Poser, B.A., Feinberg, D.A., Goebel, R., Yacoub, E., 2015. Sub-millimeter T2 weighted fMRI at 7 T:

Comparison of 3D-GRASE and 2D SE-EPI. Frontiers in Neuroscience 9, 1–14. doi:10.3389/fnins.2015.00163.

Kim, S.G., Harel, N., Jin, T., Kim, T., Lee, P., Zhao, F., 2013. Cerebral blood volume MRI with intravascular superparamagnetic iron oxide nanoparticles. NMR in Biomedicine 26, 949–962. doi:10.1002/nbm.2885.

Kolster, H., Peeters, R., Orban, G.A., 2010. The retinotopic organization of the human middle temporal area MT/V5 and its cortical neighbors. Journal of Neuroscience 30, 9801–9820. doi:10.1523/JNEUROSCI.2069-10.2010.

Koopmans, P.J., Yacoub, E., 2019. Strategies and prospects for cortical depth dependent T2 and T2* weighted BOLD fMRI studies. NeuroImage 197, 668–676. URL: https://doi.org/10.1016/j.neuroimage.2019.03.024, doi:10.1016/j.neuroimage.2019.03.024.

Lauwers, F., Cassot, F., Lauwers-Cances, V., Puwanarajah, P., Duvernoy, H., 2008. Morphometry of the human cerebral cortex microcirculation: General characteristics and space-related profiles. NeuroImage 39, 936–948. doi:10.1016/j.neuroimage.2007.09.024.

Lu, H., Golay, X., Pekar, J.J., Van Zijl, P.C., 2003. Functional magnetic resonance imaging based on changes in vascular space occupancy. Magnetic Resonance in Medicine 50, 263–274. URL: https://pubmed.ncbi.nlm.nih.gov/12876702/, doi:10.1002/mrm.10519.

Madge, V., 2020. Evaluating Voxelmorph: A learning-based 3D non-linear registration algorithm, against the non-linear symmetric normalization technique from ANTs. Ph.D. thesis. McGill University. URL: https://escholarship.mcgill.ca/concern/theses/zp38wj23v.

Malonek, D., Tootell, R.B., Grinvald, A., 1994. Optical imaging reveals the functional architecture of neurons processing shape and motion in owl monkey area MT. Proceedings of the Royal Society B: Biological Sciences 258, 109–119. doi:10.1098/rspb.1994.0150.

Marques, J.P., Kober, T., Krueger, G., Zwaag, W.V.D., 2009. MP2RAGE , a self bias-field corrected sequence for improved segmentation and T1-mapping at high field NeuroImage MP2RAGE , a self bias- fi eld corrected sequence for improved segmentation and T 1 -mapping at high fi eld. NeuroImage 49, 1271–1281. URL: http://dx.doi.org/10.1016/j.neuroimage.2009.10.002, doi:10.1016/j.neuroimage.2009.10.002.

Maunsell, J.H., Van Essen, D.C., 1983. Functional properties of neurons in middle temporal visual area of the macaque monkey. I. Selectivity for stimulus direction, speed, and orientation. Journal of Neurophysiology 49, 1127–1147. doi:10.1152/jn.1983.49.5.1127.

Moeller, S., Yacoub, E., Olman, C.A., Auerbach, E., Strupp, J., Harel, N., Uğurbil, K., 2010. Multiband multislice GE-EPI at 7 tesla, with 16-fold acceleration using partial parallel imaging with application to high spatial and temporal whole-brain FMRI. Magnetic Resonance in Medicine 63, 1144–1153. doi:10.1002/mrm.22361.

Mountcastle, V.B., 1956. Modality and Topographic Properties Neurons of Cat ' S Somatic Sensory. Education .

Mountcastle, V.B., 1997. The columnar organization of the neocortex. Brain 120, 701–722. doi:10.1093/brain/120.4.701.

Nakamichi, Y., Kalatsky, V.A., Watanabe, H., Sato, T., Rajagopalan, U.M., Tanifuji, M., 2018. 3D topology of orientation columns in visual cortex revealed by functional optical coherence tomography. Journal of Neurophysiology 119, 1562–1575. doi:10.1152/jn.00921.2017.

Oliveira, I.A., Cai, Y., Hofstetter, S., Siero, J.C., van der Zwaag, W., Dumoulin, S.O., 2022. Comparing BOLD and VASO-CBV population receptive field estimates in human visual cortex. NeuroImage 248. doi:10.1016/j.neuroimage.2021.118868.

Oliveira, I.A.F., Siero, J.C.W., Dumoulin, S.O., Zwaag, W.V.D., Zwaag, V.D., Human, O., . Improved digit selectivity using VASO-CBV in 7T digit motor mapping. Technical Report. URL: https://submissions.mirasmart.com/ISMRM2022/Itinerary/Files/PDFFiles/2112.html%0A21.

Oshio, K., Feinberg, D.A., 1992. Single-Shot GRASE Imaging without Fast Gradients. Magnetic Resonance in Medicine 26, 355–360. doi:10.1002/mrm.1910260214.

Petro, L.S., Muckli, L., 2017. The laminar integration of sensory inputs with feedback signals in human cortex. Brain and Cognition 112, 54–57. URL: http://dx.doi.org/10.1016/j.bandc.2016.06.007, doi:10.1016/j.bandc.2016.06.007.

Poser, B.A., Koopmans, P.J., Witzel, T., Wald, L.L., Barth, M., 2010. Three dimensional echo-planar imaging at 7 Tesla. NeuroImage 51, 261–266. URL: http://dx.doi.org/10.1016/j.neuroimage.2010.01.108, doi:10.1016/j.neuroimage.2010.01.108.

Rakic, P., 2008. Confusing cortical columns. Proceedings of the National Academy of Sciences of the United States of America 105, 12099–12100. doi:10.1073/pnas.0807271105.

Rees, G., Friston, K., Koch, C., 2000. A direct quantitative relationship between the functional properties of human and macaque V5. Nature Neuroscience 3, 716–723. URL: http://neurosci.nature.com, doi:10.1038/76673.

Schneider, M., Kemper, V.G., Emmerling, T.C., De Martino, F., Goebel, R., 2019. Columnar clusters in the human motion complex reflect consciously perceived motion axis. Proceedings of the National Academy of Sciences of the United States of America 116, 5096–5101. doi:10.1073/pnas.1814504116.

Shmuel, A., Yacoub, E., Chaimow, D., Logothetis, N.K., Ugurbil, K., 2007. Spatio-temporal point-spread function of fMRI signal in human gray matter at 7 Tesla. NeuroImage 35, 539–552. URL: https://www.ncbi.nlm.nih.gov/pmc/articles/PMC3624763/pdf/nihms412728.pdfhttps://linkinghub.elsevier.com/retrieve/pii/S1053811906012444, doi:10.1016/j.neuroimage.2006.12.030.

Smith, S.M., Jenkinson, M., Woolrich, M.W., Beckmann, C.F., Behrens, T.E., Johansen-Berg, H., Bannister, P.R., De Luca, M., Drobnjak, I., Flitney, D.E., Niazy, R.K., Saunders, J., Vickers, J., Zhang, Y., De Stefano, N., Brady, J.M., Matthews, P.M., 2004. Advances in functional and structural MR image analysis and implementation as FSL, in: NeuroImage. URL: www.sciencedirect.com., doi:10.1016/j.neuroimage.2004.07.051.

Sullivan, C., Kaszynski, A., 2019. PyVista: 3D plotting and mesh analysis through a streamlined interface for the Visualization Toolkit (VTK). Journal of Open Source Software 4, 1450. doi:10.21105/joss.01450.

Talagala, S.L., Sarlls, J.E., Liu, S., Inati, S.J., 2016. Improvement of temporal signal-to-noise ratio of GRAPPA accelerated echo planar imaging using a FLASH based calibration scan. Magnetic Resonance in Medicine 75, 2362–2371. doi:10.1002/mrm.25846.

Tanaka, S., Moon, C.H., Fukuda, M., Kim, S.G., 2011. Three-dimensional visual feature representation in the primary visual cortex. Neural Networks 24, 1022–1035. URL: http://dx.doi.org/10.1016/j.neunet.2011.05.005, doi:10.1016/j.neunet.2011.05.005.

Tootell, R.B., Reppas, J.B., Kwong, K.K., Malach, R., Born, R.T., Brady, T.J., Rosen, B.R., Belliveau, J.W., 1995. Functional analysis of human MT and related visual cortical areas using magnetic resonance imaging. Journal of Neuroscience 15, 3215–3230. doi:10.1523/jneurosci.15-04-03215.1995.

Triantafyllou, C., Hoge, R.D., Krueger, G., Wiggins, C.J., Potthast, A., Wiggins, G.C., Wald, L.L., 2005. Comparison of physiological noise at 1.5 T, 3 T and 7 T and optimization of fMRI acquisition parameters. NeuroImage 26, 243–250. doi:10.1016/j.neuroimage.2005.01.007.

Ugurbil, K., 2016. What is feasible with imaging human brain function and connectivity using functional magnetic resonance imaging. doi:10.1098/rstb.2015.0361.

Uğurbil, K., 2021. Ultrahigh field and ultrahigh resolution fMRI. Current Opinion in Biomedical Engineering 18. doi:10.1016/j.cobme.2021.100288.

Uludağ, K., Müller-Bierl, B., Uğurbil, K., 2009. An integrative model for neuronal activity-induced signal changes for gradient and spin echo functional imaging. NeuroImage 48, 150–165. doi:10.1016/J.NEUROIMAGE.2009.05.051.

Uğurbil, K., Adriany, G., Andersen, P., Chen, W., Garwood, M., Gruetter, R., Henry, P.G., Kim, S.G., Lieu, H., Tkac, I., Vaughan, T., Van De Moortele, P.F., Yacoub, E., Zhu, X.H., 2003. Ultrahigh field magnetic resonance imaging and spectroscopy. Magnetic Resonance Imaging 21, 1263–1281. doi:10.1016/j.mri.2003.08.027.

Viessmann, O., Polimeni, J.R., 2021. High-resolution fMRI at 7 Tesla: challenges, promises and recent developments for individual-focused fMRI studies. Current Opinion in Behavioral Sciences 40, 96–104. URL: https://doi.org/10.1016/j.cobeha.2021.01.011, doi:10.1016/j.cobeha.2021.01.011.

Virtanen, P., Gommers, R., Oliphant, T.E., Haberland, M., Reddy, T., Cournapeau, D., Burovski, E., Peterson, P., Weckesser, W., Bright, J., van der Walt, S.J., Brett, M., Wilson, J., Millman, K.J., Mayorov, N., Nelson, A.R., Jones, E., Kern, R., Larson, E., Carey, C.J., Polat, I., Feng, Y., Moore, E.W., VanderPlas, J., Laxalde, D., Perktold, J., Cimrman, R., Henriksen, I., Quintero, E.A., Harris, C.R., Archibald, A.M., Ribeiro, A.H., Pedregosa, F., van Mulbregt, P., Vijaykumar, A., Bardelli, A.P., Rothberg, A., Hilboll, A., Kloeckner, A., Scopatz, A., Lee, A., Rokem, A., Woods, C.N., Fulton, C., Masson, C., Häggström, C., Fitzgerald, C., Nicholson, D.A., Hagen, D.R., Pasechnik, D.V., Olivetti, E., Martin, E., Wieser, E., Silva, F., Lenders, F., Wilhelm, F., Young, G., Price, G.A., Ingold, G.L., Allen, G.E., Lee, G.R., Audren, H., Probst, I., Dietrich, J.P., Silterra, J., Webber, J.T., Slavič, J., Nothman, J., Buchner, J., Kulick, J., Schönberger, J.L., de Miranda Cardoso, J.V., Reimer, J., Harrington, J., Rodríguez, J.L.C., Nunez-Iglesias, J., Kuczynski, J., Tritz, K., Thoma, M., Newville, M., Kümmerer, M., Bolingbroke, M., Tartre, M., Pak, M., Smith, N.J., Nowaczyk, N., Shebanov, N., Pavlyk, O., Brodtkorb, P.A., Lee, P., McGibbon, R.T., Feldbauer, R., Lewis, S., Tygier, S., Sievert, S., Vigna, S., Peterson, S., More, S., Pudlik, T., Oshima, T., Pingel, T.J., Robitaille, T.P., Spura, T., Jones, T.R., Cera, T., Leslie, T., Zito, T., Krauss,

T., Upadhyay, U., Halchenko, Y.O., Vázquez-Baeza, Y., 2020. SciPy 1.0: fundamental algorithms for scientific computing in Python. Nature Methods 17, 261–272. URL: http://www.nature.com/articles/s41592-019-0686-2, doi:10.1038/s41592-019-0686-2.

Waehnert, M.D., Dinse, J., Weiss, M., Streicher, M.N., Waehnert, P., Geyer, S., Turner, R., Bazin, P.L., 2014. Anatomically motivated modeling of cortical laminae. NeuroImage 93, 210–220. URL: http://dx.doi.org/10.1016/j.neuroimage.2013.03.078, doi:10.1016/j.neuroimage.2013.03.078.

Watson, J.D., Shipp, S., Zeki, S., Watson, J.D., Myers, R., Frackowiak, R.S., Hajnal, J.V., Woods, R.P., Mazziotta, J.C., 1993. Area v5 of the human brain: Evidence from a combined study using positron emission tomography and magnetic resonance imaging. Cerebral Cortex 3, 79–94. doi:10.1093/cercor/3.2.79.

Weber, B., Keller, A.L., Reichold, J., Logothetis, N.K., 2008. The microvascular system of the striate and extrastriate visual cortex of the macaque. Cerebral Cortex 18, 2318–2330. doi:10.1093/cercor/bhm259.

Yacoub, E., Harel, N., Uğurbil, K., 2008. High-field fMRI unveils orientation columns in humans. Proceedings of the National Academy of Sciences of the United States of America 105, 10607–10612. doi:10.1073/pnas.0804110105.

Yushkevich, P.A., Piven, J., Hazlett, H.C., Smith, R.G., Ho, S., Gee, J.C., Gerig, G., 2006. User-guided 3D active contour segmentation of anatomical structures: Significantly improved efficiency and reliability. NeuroImage 31, 1116–1128. doi:10.1016/j.neuroimage.2006.01.015.

Zeki, S.M., 1974. Functional organization of a visual area in the posterior bank of the superior temporal sulcus of the rhesus monkey. The Journal of Physiology 236, 549–573. URL: https://onlinelibrary.wiley.com/doi/10.1113/jphysiol.1974.sp010452, doi:10.1113/jphysiol.1974.sp010452.

Zimmermann, J., Goebel, R., de Martino, F., van de Moortele, P.F., Feinberg, D., Adriany, G., Chaimow, D., Shmuel, A., Uğurbil, K., Yacoub, E., 2011. Mapping the organization of axis of motion selective features in human area mt using high-field fmri. PLoS ONE 6, 1–10. doi:10.1371/journal.pone.0028716.

Supplementary Material

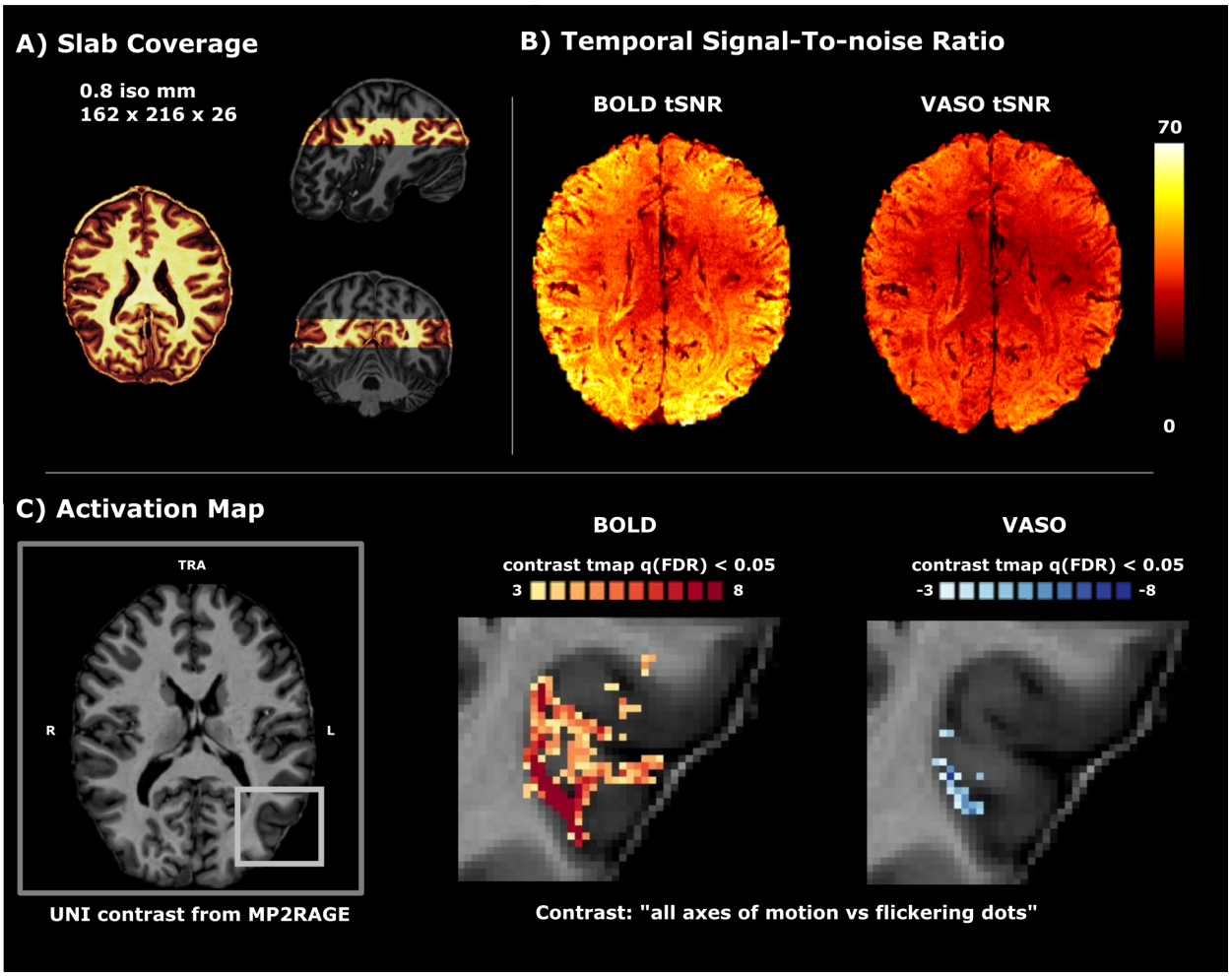

Supplementary Figure 1: SS-SI VASO functional images for an example participant (sub-01). A) Slab coverage (in warm colors) relative to a whole brain MP2RAGE. B) Temporal signal-to-noise ratio. C) Activation map for BOLD and VASO time series for the contrast: "all axes of motion vs flickering dots" (q(False Discovery Rate) < 0.05). for the left-hMT+

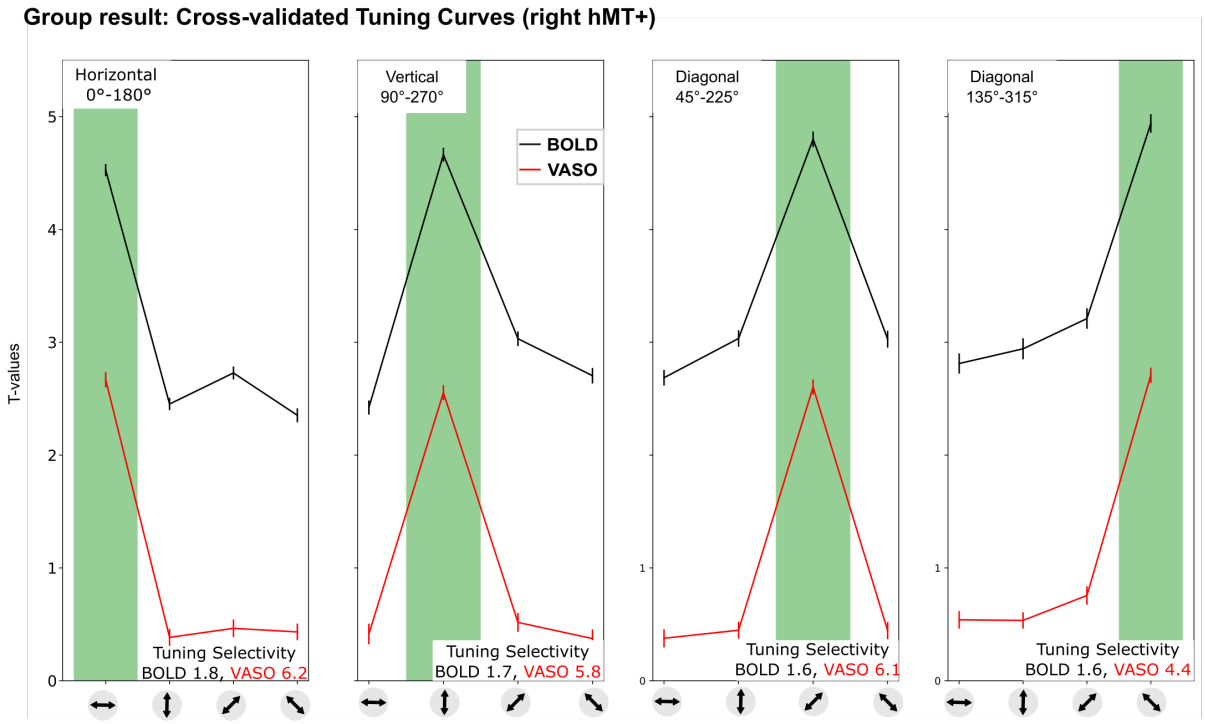

Supplementary Figure 2: Group average axis of motion selectivity tuning curves for each axis of motion for both BOLD and VASO contrast in the right hMT+. Tuning curves are computed by averaging t-values of all cross-validated (leave-one-run-out approach) voxels sharing the same preferred axis of motion. The plots depict the mean and the standard error of all voxels for each category. Tuning selectivity index is reported on the bottom of each subplot for both BOLD and VASO contrast (colors refer to the legend reported in the second column). Consistently, the VASO tuning selectivity index is higher than the BOLD one.

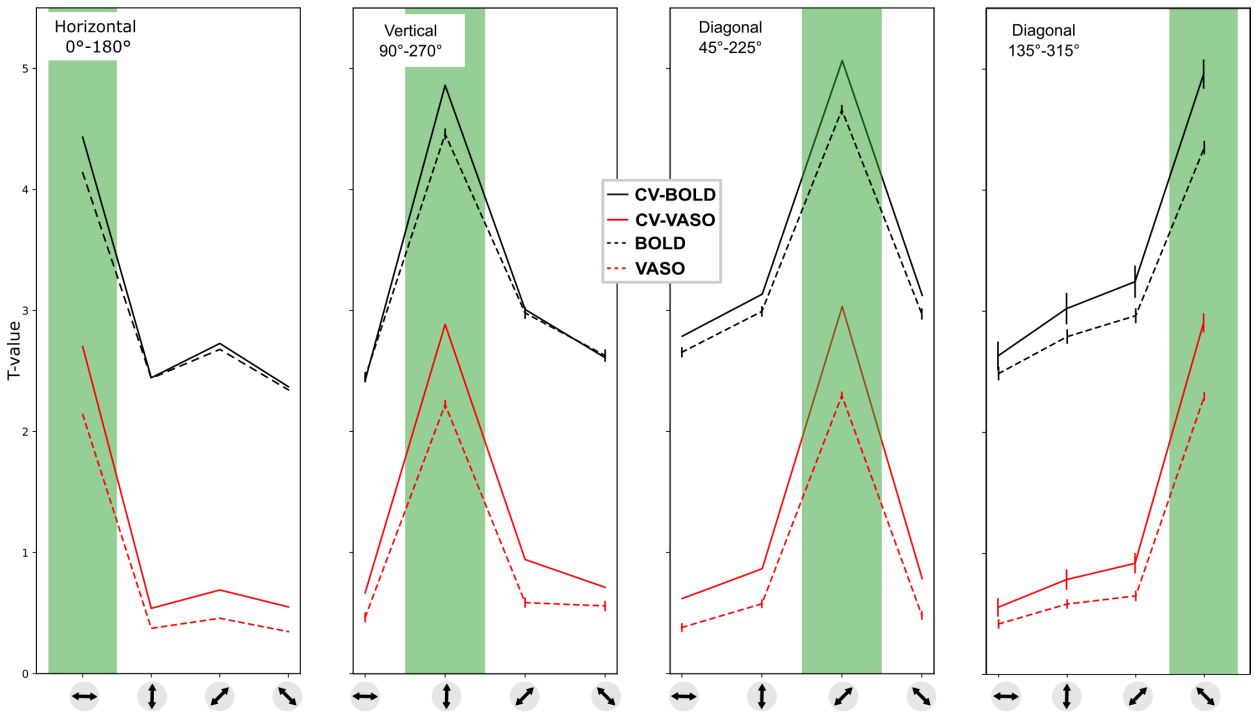

Supplementary Figure 3: Example of BOLD and VASO tuning curves before and after the cross-validation for the left-hMT+.

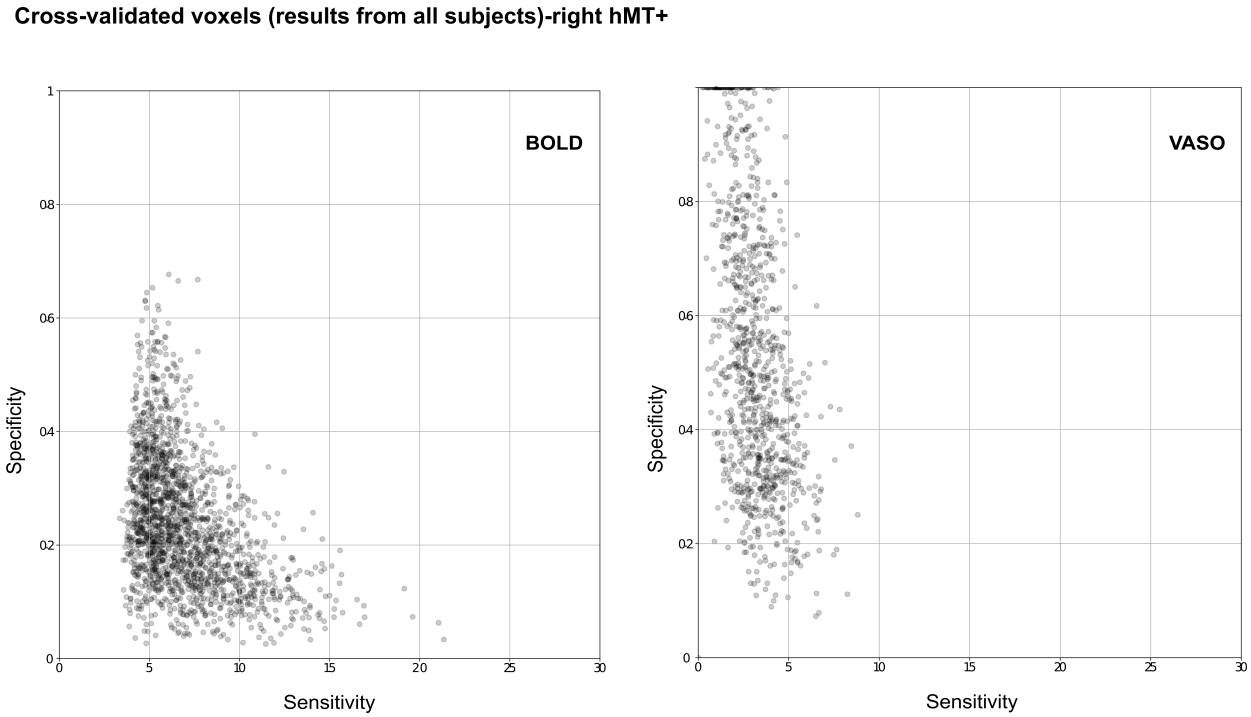

Supplementary Figure 4: Sensitivity and specificity quantify the behavior of cross-validated voxels belonging to the right-hMT+ for all participants for both BOLD and VASO contrast.

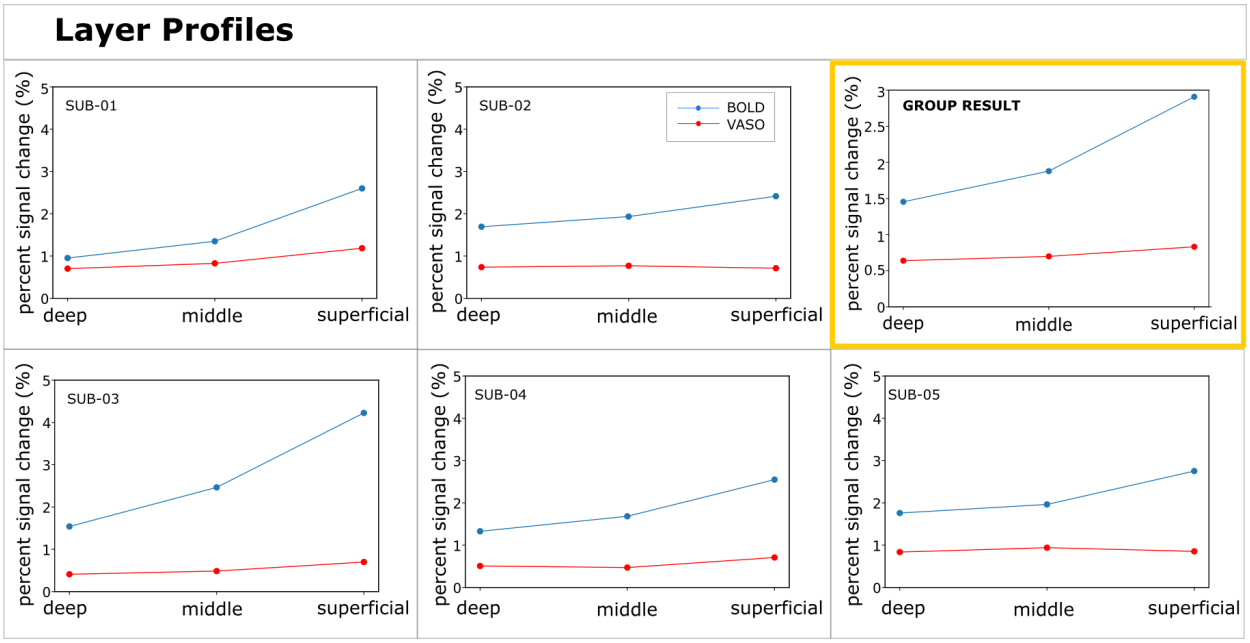

Supplementary Figure 5: Layer profiles across three cortical depths: deep (25%), middle (50%), superficial (75%) with respect to the white-gray matter boundary in the left hMT+. For each cortical depth, the averaged percent signal change of all cross-validated voxels is reported for both BOLD and VASO. The yellow box shows the group result of all five participants.

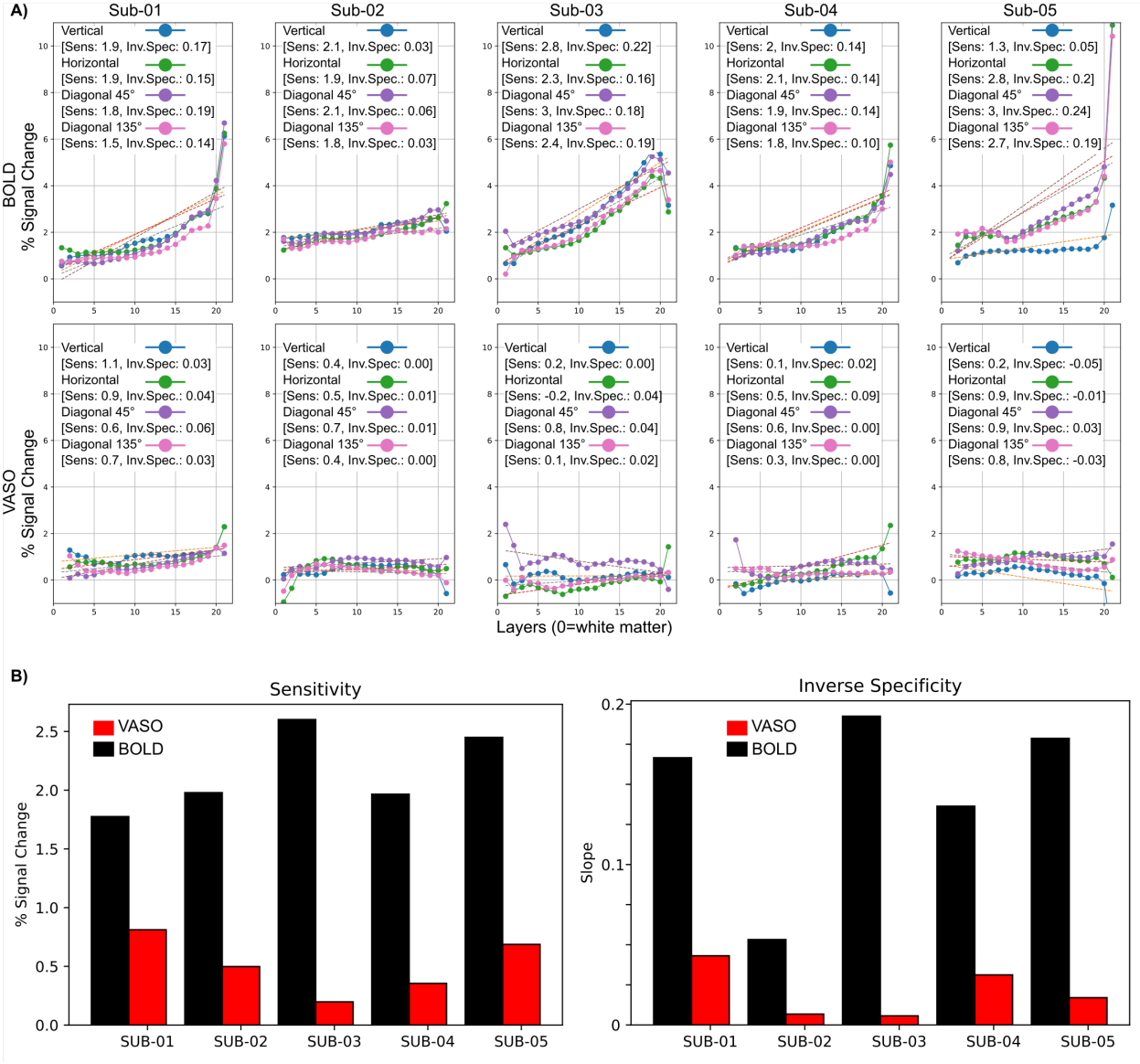

Supplementary Figure 6: Global metrics of sensitivity and inverse specificity computed for each subject (columns), for both BOLD (first row) and VASO contrast (second row) considering cross-validated voxels in the left hMT+. Each subplot shows single layer profiles for each axis of motion condition. The square brackets report global sensitivity and inverse measure of global specificity (Beckett et al., 2020). B) Global metrics of sensitivity and inverse specificity (Beckett et al., 2020) computed for each participant, for both BOLD (black bar) and VASO (red bar). Each barplot depicts the mean value evaluated across the four axes of motion.

Supplementary Table 1: Descriptive statistics for "perimeter chunk" (volume of interest used to fit the disk to compute flat coordinates) for all participants in the left hMT+. First column reports the volume in cm^3. Second column reports the radius of the disk used for each participant. The third column refers to cortical thickness measurements: mean and standard deviation is reported in curly brackets, percentage value refers to the percentage of volume whose cortical thickness measure falls in the expected range 1.5-3.5 mm. Third column summarizes the curvature measures for the volume of interest. The amount of sulcus, wall and gyrus in the region is reported as a percentage of the volume of interest.

	Volume [cm3]	Disk Radius [mm]	Thickness [mm] | [%] into [1.5-3.5] mm		Curvature sulcus | wall | gyrus [%volume]		
sub-01	1.8	15	(2.6 +/- 0.3)	98.9%	32.7	39.1	28.2
sub-02	1.1	13	(2.6 +/- 0.4)	98.4%	26.8	34.2	38.9
sub-03	1	12	(2.7 +/- 0.4)	96.9%	34.5	37.4	28.1
sub-04	1.1	13	(2.5 +/- 0.4)	97.9%	25.8	39.8	34.4
sub-05	1.9	16	(2.8 +/- 0.4)	95.7%	32	44.1	23.9